



Research article

A CFD-FFT approach to hemoacoustics that enables degree of stenosis prediction from stethoscopic signals

Ahmed M. Ali ^a, Ahmed H. Hafez ^{b,a}, Khalil I. Elkhodary ^{a,*}, Mohamed El-Morsi ^a^a Department of Mechanical Engineering, The American University in Cairo, 11835 New Cairo, Egypt^b Aerospace Engineering Department, Cairo University, 12511 Giza, Egypt

ARTICLE INFO

Keywords:

Stenosis
LES
CFD
Acoustics
Hemodynamics
Phonocardiography
Strouhal

ABSTRACT

In this paper, we identify a new (acoustic) frequency-stenosis relation whose frequencies lie within the recommended auscultation threshold of stethoscopy (< 120 Hz). We show that this relation can be used to extend the application of phonoangiography (quantifying the degree of stenosis from bruits) to widely accessible stethoscopes. The relation is successfully identified from an analysis restricted to the acoustic signature of the von Karman vortex street, which we automatically single out by means of a metric we propose that is based on an area-weighted average of the Q-criterion for the post-stenotic region. Specifically, we perform CFD simulations on internal flow geometries that represent stenotic blood vessels of different severities. We then extract their emitted acoustic signals using the Ffowcs Williams-Hawkings equation, which we subtract from a clean signal (stenosis free) at the same heart rate. Next, we transform this differential signal to the frequency domain and carefully classify its acoustic signatures per six (stenosis-)invariant flow phases of a cardiac cycle that are newly identified in this paper. We then automatically restrict our acoustic analysis to the sounds emitted by the von Karman vortex street (phase 4) by means of our Q-criterion-based metric. Our analysis of its acoustic signature reveals a strong linear relationship between the degree of stenosis and its dominant frequency, which differs considerably from the break frequency and the heart rate (known dominant frequencies in the literature). Applying our new relation to available stethoscopic data, we find that its predictions are consistent with clinical assessment. Our finding of this linear correlation is also unlike prevalent scaling laws in the literature, which feature a small exponent (i.e., low stenosis percentage sensitivity over much of the clinical range). They hence can only distinguish mild, moderate, and severe cases. Conversely, our linear law can identify variations in the degree of stenosis sensitively and accurately for the full clinical range, thus significantly improving the utility of the relevant scaling laws... Future research will investigate incorporating the vibroacoustic role of adjacent organs to expand the clinical applicability of our findings. Extending our approach to more complex 3D stenotic morphologies and including the vibroacoustic role of surrounding organs will be explored in future research to advance the clinical reach of our findings.

* Corresponding author.

E-mail address: khalile@aucegypt.edu (K.I. Elkhodary).

<https://doi.org/10.1016/j.heliyon.2023.e17643>

Received 25 November 2022; Received in revised form 20 June 2023; Accepted 23 June 2023

Available online 29 June 2023

2405-8440/© 2023 The Author(s). Published by Elsevier Ltd. This is an open access article under the CC BY-NC-ND license (<http://creativecommons.org/licenses/by-nc-nd/4.0/>).

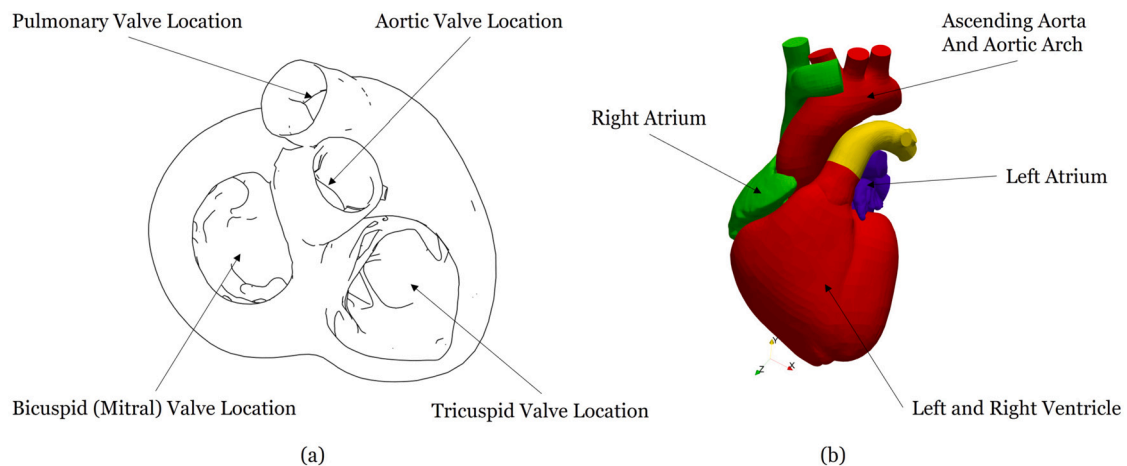


Fig. 1. Heart anatomy, per the Living Heart Human Model of Simulia, [6].

Table 1
Tools for Stenosis Diagnosis.

Method	Explanation
Echocardiogram	It uses sound waves to create images of the heart in motion. It can show blood flow through the heart and its valves, can help identify weakened heart muscles, and determine the severity of aortic valve stenosis in particular [9].
Transesophageal Echocardiogram	As above, but with a flexible tube containing a transducer that is guided down the throat and into the esophagus [10].
Electrocardiogram (ECG or EKG)	Detects and records heart electrical activity. It can detect enlarged chambers and abnormal heart rhythms [11].
Chest x-ray	Shows if there is a significant change in the heart chambers or aorta size.
Computed Tomography (CT) scan	Combines Several images to provide more comprehensive views of the heart [12].
Magnetic Resonance Imaging (MRI)	It uses a magnetic field to create detailed images of the heart. An advancement is 4D MRI, which further reveals heart motion in time [13].
Catheterization	When the above methods do not reveal a clear diagnosis, an invasive method that involves inserting a thin tube (catheter) through a blood vessel and guiding it to the heart to measure the pressure inside different regions of the heart [14].

1. Introduction

Stenosis refers to the condition where an obstruction exists inside a passage wherein fluid flows. We here focus on stenosis in the cardiovascular system; see Figs. 1a and 1b, which locate its major components in the axial and front views, respectively. Various phenomena could cause stenosis, e.g., stenosis due to a heart valve's open state becoming narrowed by calcification of its leaflets or stenosis due to a narrowing of a blood vessel just above the valve (Super-Supra [1], [2]), or stenosis due to depositions elsewhere along an artery (e.g., aortic, coronary arteries), e.g., due to atherosclerosis, where fat deposits in clusters on the walls of blood vessels [3], [4]. Cases of stenosis are considered mild when an obstruction is less than 40%, moderate when obstruction ranges between 50% and 60%, and high, or hemodynamically relevant when exceeding 70%, in which case angioplasty may often be required [5]. As such, early cases of stenosis can easily go undetected.

Early diagnosis of a stenotic condition can be vital since severe vascular blockage can be fatal [7]. As a first screening, today's medical practice relies on identifying heart-related issues by listening for changes in normal heart sounds [8], e.g., looking for murmurs with a stethoscope during physical examinations, unless symptoms warrant more detailed, expensive, and less-widely available diagnostic methods. For such cases, clinicians could turn the patient to more advanced diagnostics, such as those listed in Table 1, which can more accurately help diagnose a patient's heart condition.

Similarly, clinicians can request phonoangiography for symptomatic patients. Phonoangiography requires a computer-assisted device fitted with an advanced sensor to identify what are commonly called bruits, i.e., changes in the sound of blood as it flows through a narrowed portion of an artery [15]. These investigations do not typically quantify the exact degree of stenosis but can classify cases as mild, moderate, or severe [16–21].

In the absence of sufficiently concerning symptoms, however, a patient would not benefit from the insights offered by such advanced diagnostics since their cost and inconvenience would not be regularly justified. Consequently, the chances of accurately diagnosing asymptomatic or mildly symptomatic heart problems (e.g., low to moderate stenosis) do not match the state-of-the-art of modern clinical capability. Indeed, it is widely recognized in the literature today that there remains much room for enhancing existing diagnostic and therapeutic procedures to improve the treatment of stenosis [22]. We thus want to explore in this paper how first screenings with a stethoscope (auscultations) could yield more powerful diagnostic assessments that better support clinical decision-making, particularly regarding early and accurate assessments of stenosis.

We turn our attention to in-silico studies for related cardiovascular research objectives, as they have become increasingly common, especially for their ability to offer quantitative insights into the mechanisms that underly the clinical phenomena observed in-vivo at the organ level, e.g., [6,23].

Specifically, several computational works in the literature explicitly considered the study of generating and analyzing virtual phonocardiograms. For instance, the authors of [24] simulated a phonocardiogram by modeling the left ventricle and the ascending aorta during systole. Their primary focus was on ventricular hypertrophy, creating stenotic conditions at the start of the ascending aorta. In their simulations, they identified complex vortex structures and stated that “complex vortex” structures are the source of murmurs. Their findings are consistent with those of [25], whose authors solved for 3D stenosed pipes using DNS and reported “instantaneous coherent structures”, i.e., vortices behind the stenotic region. Similarly, the authors of [26] used CFD to identify a close relationship between jet shear layer and acoustic refraction. Again, the authors of [27,28] analyzed phonocardiograms by applying their different computational methods and have succeeded in classifying the degree of severity of coronary artery disease or the signature of mechanical heart valves. Moreover, the authors of [29] applied neural networks to learn patterns in the phonocardiograms and map them back to available heart sound databases (PASCAL and PhysioNet 2016) with remarkable accuracy.

Of special relevance to our study is work by [24,30,31]. They successfully identify computationally scaling laws for moderate and severe degrees of stenosis, as well as its likely location, based on the concept of the *break frequency*. A break frequency is obtained by solving for the spectrum of acoustic frequencies generated by the bruits and post-processing for an observed frequency where the slope of the spectrum changes significantly. This frequency has been reported to arise in a range that may be better suited for phonoangiography, e.g., [18], but not for stethoscopes (< 120 Hz), cf., [32], which motivates our research to identify another frequency that can be stethoscopically associated with bruits.

We thus turn our attention to other related in-silico studies to confirm that CFD is an adequate method for our targeted clinically relevant in-silico investigations, capable of in-depth quantitative analysis of further flow characteristics that could associate with the bruits. We found that is the case, but with some caution about the details of the CFD method.

For instance, [33] conducted a detailed computational fluid dynamics (CFD) analysis of blood flow in large arteries, successfully demonstrating quantitatively how the cardiovascular circulation impacts the morphological characteristics of visceral muscular arteries. Along a similar path, [34] investigated by CFD how blood pressure and velocity at a carotid bifurcation affect its walls to increase the risk of disease. Also, [35] used CFD to compute wall shear stress and pressure drop in the blood in relation to aortic tortuosity to help inform subsequent surgical intervention, while [36] used CFD to investigate a specific surgical intervention, i.e., the Left Ventricular Assist Device (LVAD), in relation to obtaining optimal hemodynamics for a patient. As such, CFD simulations have been repeatedly shown to be reliable for clinical assessments. Nevertheless, [37,38] accounted for the circumferential strain of the blood vessels by extending their CFD analysis to include fluid-structure interaction (FSI). While FSI demonstrated the importance of aortic wall elasticity in severe stenosis cases, it did not yield additional insight for mild to moderate stenosis cases, suggesting the adequacy of CFD for most of the stenotic range. We will thus suffice our study with CFD simulation in lieu of FSI.

Despite these reported findings and similar progress in clinically relevant CFD, the authors of [39] reviewed the details of the CFD method as it is applied within cardiovascular applications and pointed out that in areas that relate to the accurate modeling of the aorta, there remains room for improvement. We will detail key improvements in our methods section.

Indeed, [40] showed that different CFD solvers could generate different results for the same problem, varying to the degree that the results are unsuitable for clinical use. A careful choice of CFD solver and its settings is thus in order. In that vein, the authors of [41] considered turbulent pulsatile flow in stenotic vessels by comparing the RANS (Reynolds Averaged Navier Stokes) model with DNS (Direct Numerical Simulation) and LES (Large Eddy Simulation), all being valid alternatives commonly used by CFD modelers today. They showed that RANS, paired with k-omega turbulence modeling, agrees in its average fields with the more expensive and accurate DNS and LES simulations [42]. Nevertheless, with today's advancement in computational resources, LES modeling still offers a better alternative for its ability to resolve the evolving fluid structures when compared with RANS, which justifies its extra computational cost, especially when complex flow patterns (and their associated acoustic signals), are essential to the analysis, cf. [31] who perform a successful 2D flow analysis of stenosis using LES to identify the break frequency. Moreover, the authors of [43] used LES to solve for the acoustic field in a T-shaped pipe. They succeeded in resolving the acoustic frequency of the flow and identifying its dependency on the position of the source of the sound. Also, the authors of [44] explored a fully developed turbulent flow inside a roughened 3D pipe, using RANS and LES, again confirming the need for LES to resolve the fluid flow field. Nevertheless, a RANS k-omega approach remains valuable to studying stenosis, specifically as a practical CFD technique when running expensive FSI simulations. For instance, [45] paired their FSI to RANS k-omega to study wall shear stress for varying degrees of stenotic severity (30%, 50%, and 70%), concluding that stenosis increases blood velocity and (detrimentally) wall shear stress, consistent with the findings presented in [46]. Since lowering the FSI computation cost is irrelevant to our study, we will adopt LES.

Another important aspect of correctly performing CFD simulations of the cardiovascular system is the nature of the inlet flow of its vessels, cf. [47]. We note that blood is mixed and pumped from the left ventricle, through the aortic valve, and into the ascending aorta, in a turbulent and pulsatile fashion. The authors of [48] specifically investigated the influence of pulsation on flow transition from a laminar to a turbulent regime. They introduced puffs, i.e., small induced turbulences, to their inlet flow and observed that these aided in flow transition to the turbulent regime. For proper cardiovascular flow modeling, similar puffs should always be accounted for at the vessels' inlets to capture existing patterns of turbulence near the valves and their ultimate influence on the resulting acoustic signal. A similar conclusion was also reached by [49] and [50].

Following this path, we perform CFD analyses of flow inside a stenotic ascending aorta, capturing different degrees of stenosis. Our research objective is to take hemoacoustics a step further by quantitatively correlating the degree of stenosis to auscultated frequencies within the stethoscopic best range so that stethoscopes could become a more powerful diagnostic tool extending the

benefit of phonoangiography. We will thus analyze in fuller detail than the literature the spatiotemporal patterns of stenotic flow generated by CFD (LES). We will classify a narrow frequency spectrum based on fast Fourier transforms (FFT), which is the signature of the von Karman Street, to find a new dominant acoustic frequency of vortex shedding that differs from the break frequency and lies below the 120 Hz range. We reveal a continuous linear relationship between stenotic degree and this new vortex shedding frequency. This frequency will be shown to be consistent with the original definition of the Strouhal number [51].

The novelty of this work can be summarized as follows. While bruits have been known to relate to vortex shedding and have been long understood to correlate with the degree of stenosis, previous correlations have been identified via the concept of a break frequency, as originally identified via phonoangiograms [18], and computational studies have remained true to this concept, e.g., [52]. The limitation of the break frequency is that it lies beyond the best range for stethoscope-based clinical diagnoses of critical heart sounds (70-120 Hz) [32], rendering its identification reliant on sophisticated sensors and computer-assisted devices. Our paper introduces an alternative frequency definition that restricts the acoustic spectrum to the formation of the von Karman vortex street, identifying this phase of flow automatically by means of the Q-criterion. We perform a spectral analysis for this phase's acoustic signature using FFT and show that its dominant frequency yields a strong positive correlation with the degree of stenosis. Importantly, this new frequency differs considerably from the break frequency, being well below the 120 Hz threshold for all stenosis cases (mild to severe), rendering it suitable for stethoscope-based diagnoses. We further remark that the scaling laws in literature which are based on the break frequency have only limited sensitivity to clinical variations in degree of stenosis, featuring exponents as low as 0.1 [31]. As a result, exact quantification of the degree of stenosis has remained elusive using those laws, and only classified as mild, moderate or severe. However, our work herein quantifies a linear correlation using our proposed frequency, which permits an exact and continuous quantification of stenosis degree.

2. Methods

Fluid flow structures in blood vessels behind stenotic regions, i.e., vortices or eddies, are reckoned to be typical causes for a change in normal heart sound. We here lay out a methodology to create a database of stenotic geometries of clinical relevance and a corresponding database of simulated acoustic signals. Using these databases, we can then define a correlation between the degree of stenosis and dominant phonocardiographic frequency. Clinicians can then, in principle, benchmark their stethoscopic auscultations against the correlation we identified in this work to noninvasively and with accuracy determine the degree of stenosis presenting in a patient during standard physical examination.

Our proposed methodology is summarized graphically in Fig. 2. We start by considering a stenotic geometry from the ascending aorta. We idealize the stenosis as a sharp-edged obstruction, as shown in the figure. CFD calculations are then performed using LES for three cardiac cycles to ensure that the results for a given cardiac cycle are indeed repetitive. A thorough analysis of the velocity and pressure fields then ensues to identify the onset and termination of the various phases of flow within the cardiac cycle; we here identify *six* phases, as explained shortly. Of particular interest is the fourth phase, where a vortex train, i.e., the von Karman vortex street [53], appears and endures. The acoustic signal for the entire cardiac cycle is thus obtained. A second acoustic signal for a clean case (non-stenotic) is also computed. These two acoustic signals are subtracted, and the resulting differential is segmented and clipped for the time duration of the vortex train. A Fast Fourier Transform (FFT) is then applied to this segment of the differential acoustic signal to obtain the dominant acoustic frequency of the train, which represents the (auscultated) Strouhal frequency of vortex shedding. Repeating these steps for the various stenotic geometries reveals a linear correlation between the dominant acoustic frequency of vortex shedding and the degree of stenosis. We validate our correlation against the differential of available clinical phonocardiographs and clarify how clinicians expect it to be employed during physical examinations to quantify the severity of stenosis, even for cases that may be asymptomatic (mild to moderate). The following subsections further detail our methodology.

2.1. Pre-processing: CFD model setup

Pre-processing involves setting up representative geometric models of stenotic flow, selecting an applicable governing law and its corresponding solver on commercial CFD software (Ansys), applying appropriate boundary conditions that match solver needs, and then meshing the flow domain repeatedly to obtain a convergent mesh.

2.1.1. Geometry modeled for stenotic flow and acoustic signal

A 2D flow domain is used per Fig. 3, representing an idealized ascending aorta, beginning from the aortic valve and ending at the beginning of the transverse arch. The domain is modeled as a straight tube, where stenosis has an axial width of 6 mm in all cases, with percentage stenosis (degree of blockage) changing from 30% to 80% (i.e., mild to severe), which we model in increments of 10%. The aortic diameter is set at 20 mm, based on the clinical study conducted by [54], which found this value representative of average young adults. The location of the stenotic region within the modeled domain is shifted to the left to permit full-flow development behind the stenotic region. Our stenosis models herein are also consistent with those used by [24] and [25]. A model with no stenosis is also included in our database for later signal differencing. The blood vessel is, in all simulations, surrounded by a domain with static air that permits sound propagation from vessel walls. The surrounding domain also contains a sound receiver at the top right corner, where the emitted acoustic signals from the vessel walls are integrated for subsequent analysis, see Fig. 3.

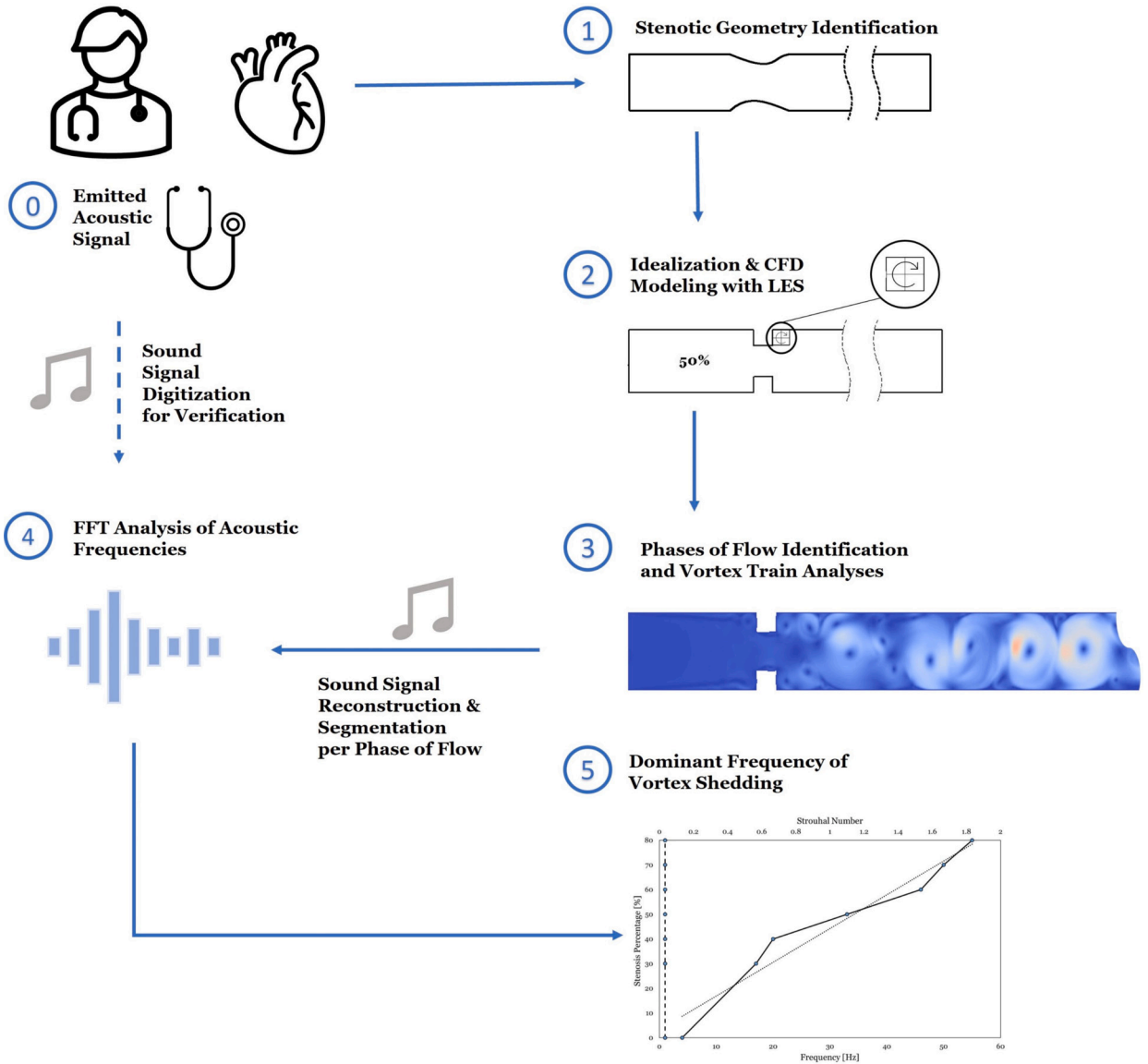


Fig. 2. Methodology Proposed to Reveal Unknown Correlations between Emitted Phonocardiographic Frequencies and Stenotic Geometries.

2.1.2. Selecting the governing laws and the solver

The typical governing equations for CFD simulations are the mass continuity equation (Equation (1)), and the Navier Stokes (momentum) equation (Equation (2)), shown below.

$$\nabla \cdot u = 0 \tag{1}$$

$$\rho(\partial u / \partial t + (u \cdot \nabla)u) = -\nabla p + \nabla \cdot ((\mu + \mu_t)(\nabla u + (\nabla u)^T)), \tag{2}$$

In Equations (1) and (2), u designates the fluid's flow velocity, ρ its density, μ its kinematic viscosity, and μ_t the eddy viscosity, or turbulent viscosity. We assume isothermal flow conditions to avoid solving the energy balance equation.

As remarked earlier, an LES solver will be used herein to solve these governing equations since it offers a good trade-off between computational resources (relative to DNS, cf. [55,56]) and flow-field resolution accuracy (relative to RANS); see Fig. A.1 for a clarification of how RANS falls short relative to LES based on an example from the present study. LES is thus best suited for our intended acoustic analysis.

The basic idea behind LES is its recognition that turbulent flow contains eddies that span a range of sizes and corresponding energies. LES is thus set up to *explicitly* resolve only the upper sub-range of these eddies. The upper range depends on the mesh size selected (implicit filtering). It recognizes that a minimum of four cells (i.e., two-by-two in 2D) is needed to resolve a given eddy

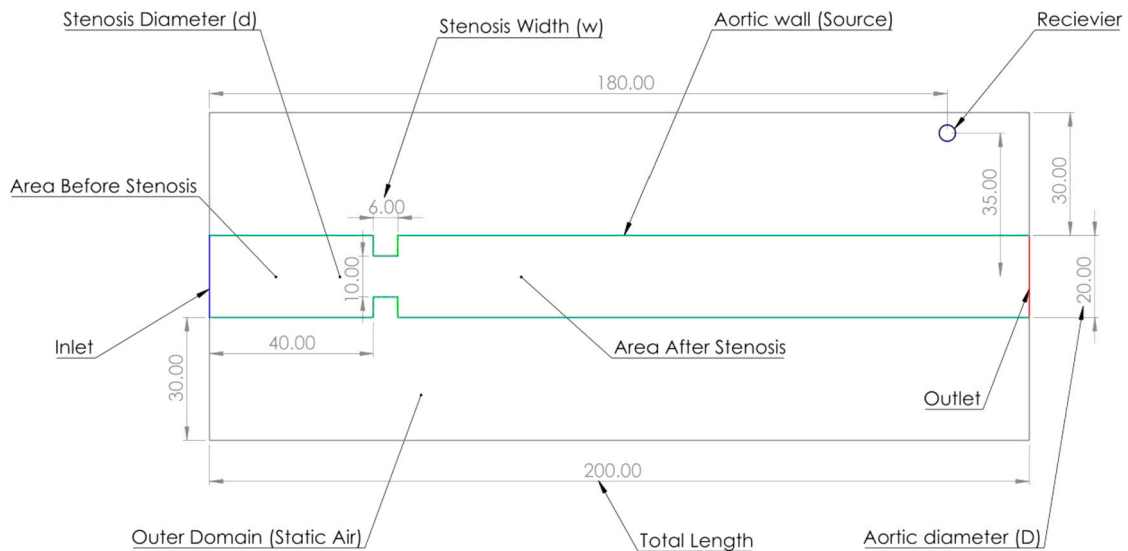


Fig. 3. 2D flow domain representing a stenotic ascending aorta, for the case of 50% stenosis. A domain of stagnant air encloses the stenotic domain to permit sound propagation. The circle on the top right corner denotes the receiver's location. Stagnant air is at room temperature (289 K). All dimensions listed are in mm.

Table 2
Model Clinical & Engineering Assumptions.

Clinical Assumptions	Engineering Assumption
Blood density = $1060 \frac{\text{Kg}}{\text{m}^3}$	Pulsatile (unsteady flow)
Blood viscosity = $0.00278 \frac{\text{kg}\cdot\text{m}}{\text{s}}$	Turbulent, viscous, transient, incompressible, and isothermal flow conditions.
The patient exhibits a resting heart rate of 1 cardiac cycle per second.	Turbulence (puffs) is introduced at inlet flow (spectral synthesizer). Spatially uniform velocity across the inlet.
Surrounding tissue effects on the acoustic signal generated are excluded.	Newtonian flow assumed for this large artery modeled, where shear rate is above 100 sec^{-1} , and with constant dynamic viscosity.
The gravity effect is neglected.	No slip condition at the walls (which are rigid).

explicitly. For smaller eddies, a sub-grid scale model that *implicitly* captures their effect on the flow is incorporated into the LES formulation (i.e., for eddies smaller than a width of 2 cells in the mesh).

Moreover, to resolve the near-wall flow behavior, the length scale for the mesh cells near the wall should be much smaller than that in the domain's center. To alleviate this requirement, we here select the WMLES S-omega model, where WMLES stands for Wall Modeled LES, which computes wall-bounded flows without requiring a significant increase in grid resolution near the walls, with S-omega being an enhancement to WMLES that captures transitional effects. Further details may be found in the Ansys Fluent Theory Guide.

In Table 2, we list the clinical and engineering assumptions we made while setting up our WMLES model of stenotic flow on Ansys. Our data are consistent with various sources in the literature, cf. [45], [57], [41], [58], and [59].

2.1.3. Boundary conditions

The boundary conditions (BCs) for any CFD simulation consist of inlet and outlet conditions. A time-dependent inlet waveform, per [60] and [61], is used to generate the underlying pulsatile flow pattern at the inlet. On setting our inlet BC, we introduced artificial turbulence (puffs) as a fluctuating velocity, based on the work of [48]. The intensity of these fluctuations was heuristically specified at a value of 5%, and the hydraulic diameter was taken to correspond to the inlet diameter. The spectral synthesizer on Ansys takes these two values as input and generates the desired puffs, as clarified in Fig. 4, which shows the velocity profile at the inlet for the 50% stenosis case at different times of the cardiac cycle; specifically, Figs. 4(a), 4(b), and 4(c) correspond to 0.2 s, 0.6 s, and 1 s, respectively.

Conversely, the outlet BC was defined simply as a static pressure corresponding to diastolic pressure, i.e., 80 mmHg [61], for the duration of the simulation.

2.1.4. Meshing

Ansys Fluent's mesher (Mechanical) was used herein to create the mesh. Quad4 elements were used. Fig. 5a illustrates the mesh near the stenotic region, and Fig. 5b zooms at the near-wall mesh. Each stenosis case corresponds to a different diameter, so the element count varies from case to case. A boundary Layer (inflation region) of 0.5 mm on both the upper and lower walls was introduced in all models, see the zoom-in in Fig. 5, to permit a higher resolution of flow structures near the wall with LES, and to

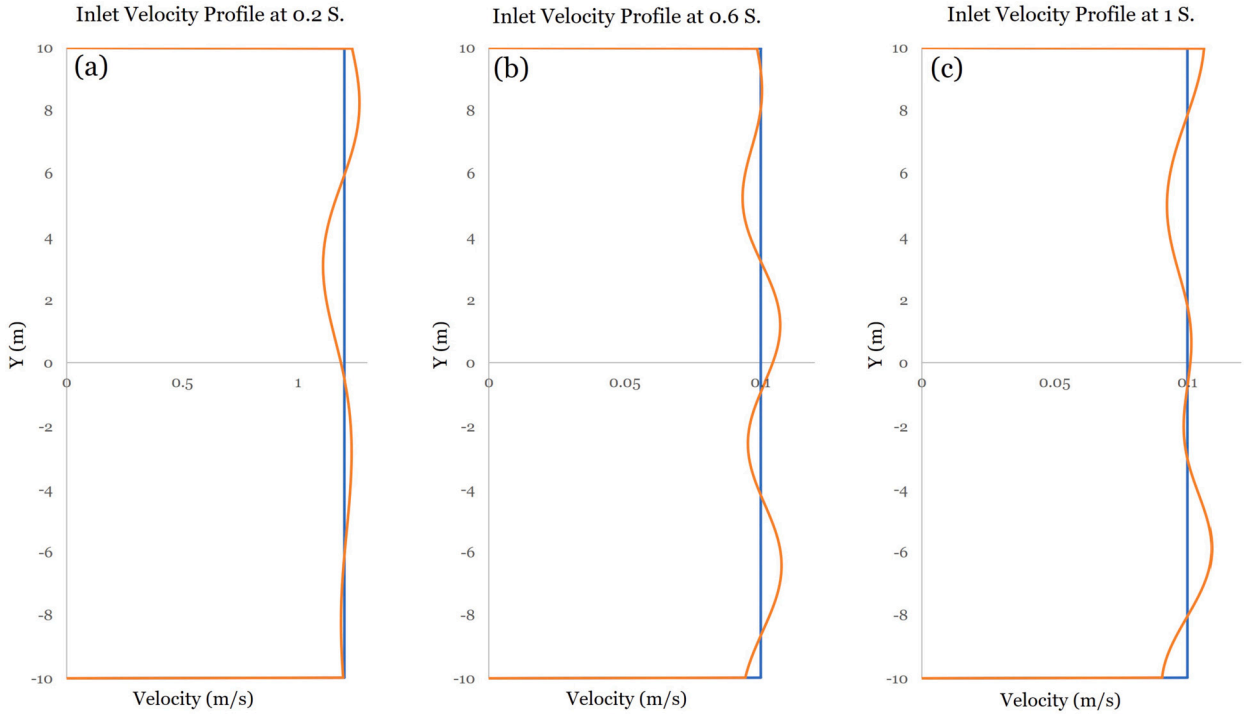


Fig. 4. Inlet velocity profile at different time frames, clarifying the effect of using a spectral synthesizer at the inlet at different times, (a)-(c).

minimize errors that arise from the implicit capturing of length scale structures. As a result, the average number of nodes is 816,000, and the corresponding number of elements is 814,100.

2.2. Running the LES simulation

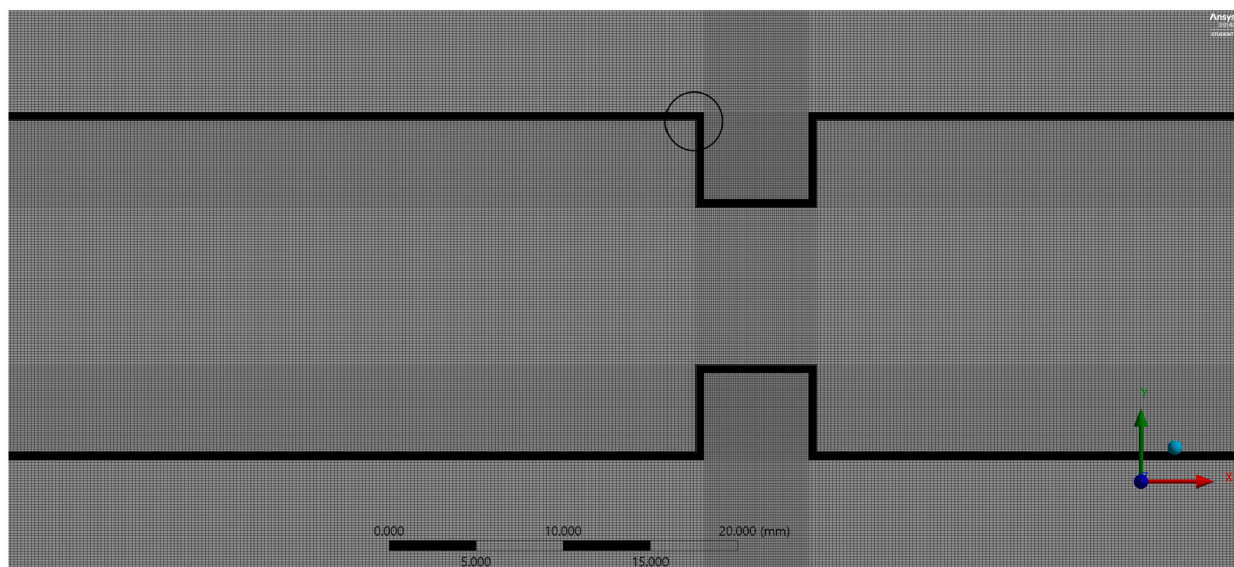
To run our LES simulations, the computing power that we used benefitted from solver parallelization [62], employing 24 AMD Opteron Processor (6174) CPUs and 12B GB of RAM. Each simulation ran for approximately 14 hours on Ansys Fluent, Release 19.3. We note that our choice of CFD solver will not impact the clinical relevance of our predictions, as has been demonstrated in the literature [40] for simple geometries (similar to our models). We selected the simple scheme for pressure-velocity coupling on ANSYS and the bounded second-order implicit transient formulation. Iterations proceeded until residuals in the mass continuity and momentum equations reached 10^{-4} . Time stepping was selected after various numerical tests, and a time increment of 0.0002 s was found reasonable for solution stability and rate of convergence. We ran different stenotic simulations for up to five cardiac cycles. We found that the flow structures that evolved behind the stenotic regions showed no significant change from cycle to cycle. As such, we recommend that only two cycles be run for the practicality of analysis, with a total number of 10,000-time steps. The second cardiac cycle is needed to generate the acoustic signal per ANSYS, as discussed below.

2.3. Post-processing: acoustic signal generation

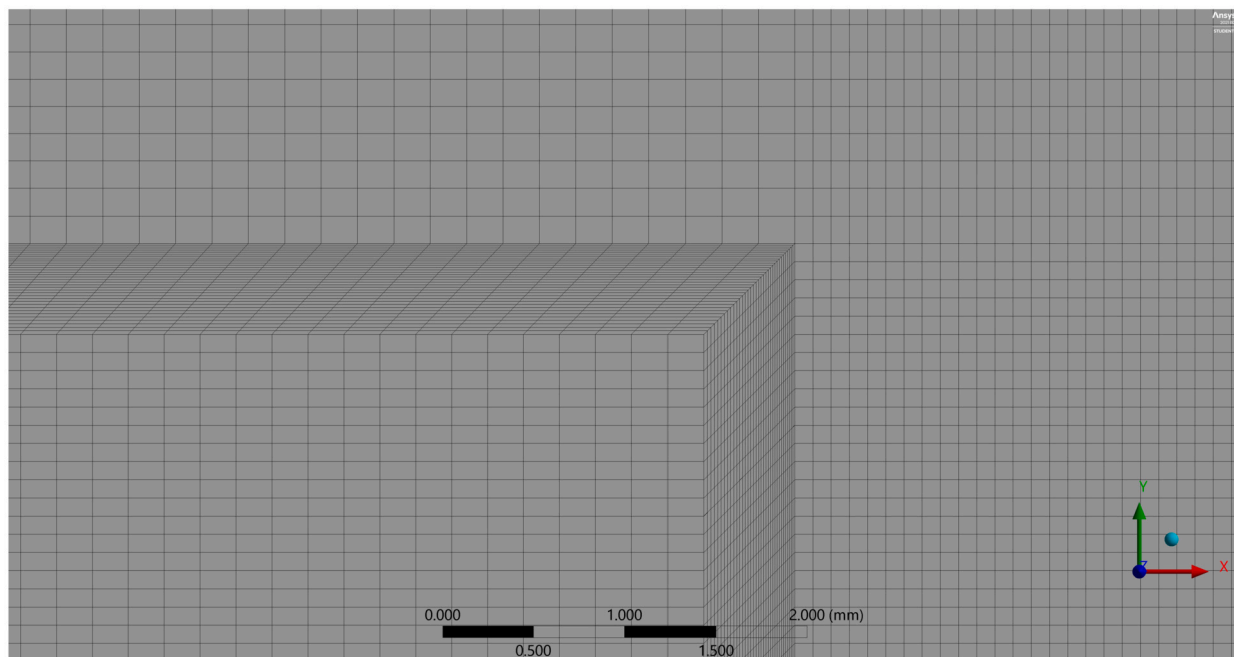
One of the methods to capture mid- to far-field noise signals that are implemented on ANSYS is the Ffowcs William-Hawkings (FW-H) method [63,64]. Our modeled domain in Fig. 3 can be separated into two solution domains; the flow field (blood flow), whose walls act as the source of sound for its surroundings, and the acoustic field (with static air), where sound propagates off the walls, following the wave equation. The two domains are connected using the Lighthill analogy, upon which the FW-H method is based. Specifically, the FW-H equation (Equation (3)) is an inhomogeneous wave equation that derives from continuity and Navier Stokes,

$$\begin{aligned} \frac{1}{a_0^2} \frac{\partial^2 p'}{\partial t^2} - \nabla^2 p' &= \frac{\partial^2}{\partial x_i \partial x_j} \{T_{ij} H(f)\} \\ &- \frac{\partial}{\partial x_i} \{ [P_{ij} n_j + \rho u_i (u_n - v_n)] \delta(f) \} \\ &+ \frac{\partial}{\partial t} \{ [\rho_0 v_n + \rho (u_n - v_n)] \delta(f) \} \end{aligned} \quad (3)$$

where, u_i designates fluid velocity in direction x_i , u_n the fluid's velocity normal to the surface, v_i the surface velocity component in direction x_i , and v_n the surface velocity component normal to the surface. $\delta(f)$ denotes the Dirac delta function, $H(f)$ the



(a)



(b)

Fig. 5. (a) The mesh for the case of 50% stenosis. (b) Zoom-in reveals the higher mesh density near the wall.

Heaviside step function, and $f = 0$ denotes the function that describes the wall which emits sound. The following parameters were correspondingly selected to nondimensionalize our acoustic analysis: the far field density away from the aorta is set to 1.225 kg/m^3 , and the far field speed of sound away from the aorta is set to 340 m/s , the free stream velocity away from the aorta is set to 0 m/s , and the reference acoustic pressure away from the aorta is set to $2 \times 10^{-5} \text{ Pa}$. Hence, the sound pressure level will be measured herein in dB. The acoustic power is set to 4×10^{-10} for the air domain and 1×10^{-12} for the blood domain. Finally, along the depth-wise direction, a Source Correlation Length of 0.085 is defined for the FW-H integral.

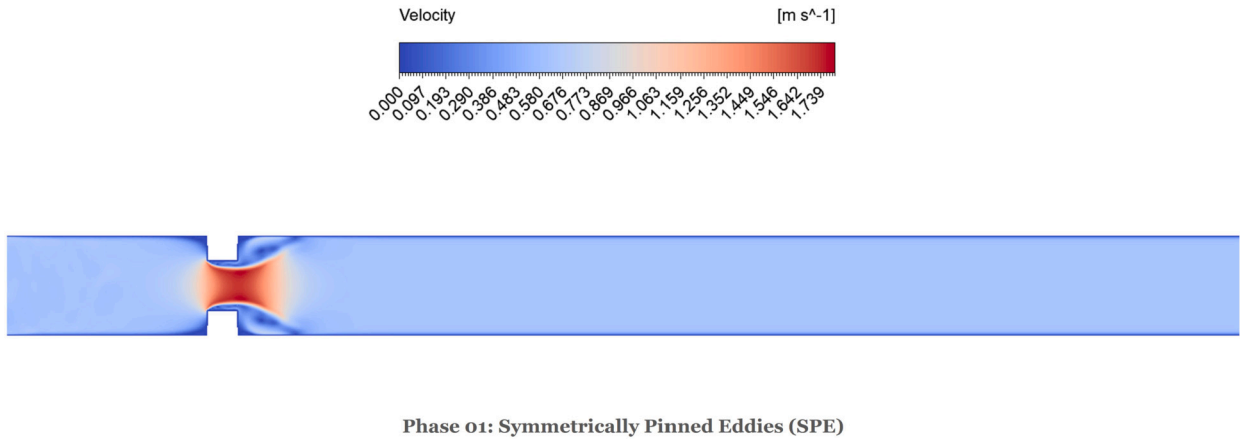


Fig. 6. Symmetrically Pinned Eddies phase. It starts at 0.02 sec and ends at 0.06 sec, in general.

3. Results

This section is organized into two parts. The first part analyzes the spatial patterns of flow, or phases of flow, which we identified behind the stenotic region for a given cardiac cycle. The second part presents our analysis of the acoustic signals obtained for each stenosis case and highlights the need for a rigorous calculation of the Strouhal number.

3.1. Stenotic flow structure classification

CFD simulated pressure and velocity fields are inspected visually throughout the second cardiac cycle to monitor the apparent evolution in fluid flow structures, specifically those found to repeat for different degrees of stenotic severity. Once a flow pattern is identified, its start and end time frames are visually marked for later spectral analysis. This visual inspection was performed on all the cases of stenosis (30% to 80%, at increments of 10%).

The case of 50% stenosis is presented here for a detailed illustration. As can be seen from Figs. 6, 7, 8, 9 and 11 and Fig. 12, the flow patterns that evolve over a cardiac cycle can be divided into six identifiable structures or flow phases. Their labels and characteristics are outlined below.

Symmetrically Pinned Eddies (SPE). Two eddies form symmetrically to either side of the stenosis on its downstream end; see Fig. 6. This phase has already been documented in the literature, though no specific label has been assigned to it, and has been shown to occur behind sharp internal flow obstacles, cf. [65,66]. The stenosis in our model is a symmetric obstruction, hence the symmetry of the pinned eddies. As we progress in time, these eddies grow larger in diameter and only drift slowly along the domain's axial direction towards the outlet. For high stenosis, these eddies also visibly drift laterally in the direction of the wall, attempting to occupy the region on the backside of the stenosis. These eddies remain more or less pinned in their position between 0.02 and 0.06 seconds of the 1-second cardiac cycle. The space they occupy leaves a reduced area for net forward flow, increasing the axial velocity at the center of the flow, which lasts for the duration of this SPE phase.

Symmetric Eddy Propagation (SEP). This flow phase designates an axially symmetric propagation of the eddies, which formed during the SPE phase, toward the flow domain's outlet; see Fig. 7. We note that this phase lasts between 0.06 and 0.1 seconds. We could not identify its mention in the literature, however. As such, we deem it a previously undocumented stenotic flow phase detail revealed by our present LES analysis.

Asymmetric Eddy Propagation (AEP). This flow phase designates a loss to the propagating eddies' axial symmetry as they continue their axial motion; see Fig. 8. This AEP phase lasts between 0.1 and 0.2 seconds and is also undocumented in the literature on stenotic flow but is revealed as a new detail on stenotic flow phases by this LES analysis.

Karman Vortex Street (KVS). This phase is well documented in the literature, cf. [65,67–69]. For the case of mild stenosis, the train develops some distance away from the inlet, as compared with severe stenosis, where the train dominates the post-stenotic domain; see Fig. 9. For all stenosis cases, the KVS phase starts at 0.2 s and ends at 0.4 s. Given the importance of the KVS phase, specifically in relation to our subsequent acoustic analysis, we have identified that its timing is best captured by the area-weighted average of the Q-criterion [70],

$$Q_{norm} = \frac{\text{Max}[0, \frac{1}{2}\Omega^2 - S^2]}{\frac{1}{2}\Omega^2 + S^2}, \quad (4)$$

Where Ω is the skew-symmetric part of the velocity gradient and S is its symmetric part. By averaging this Q-criterion (Equation (4)) over the post-stenotic region, see Fig. 10 for the case of 60% stenosis; we find its trend increases (the slope becomes positive) between 0.2 and 0.4 seconds. This increase corresponds to the situation where the flow's rotation rate grows relative to the strain

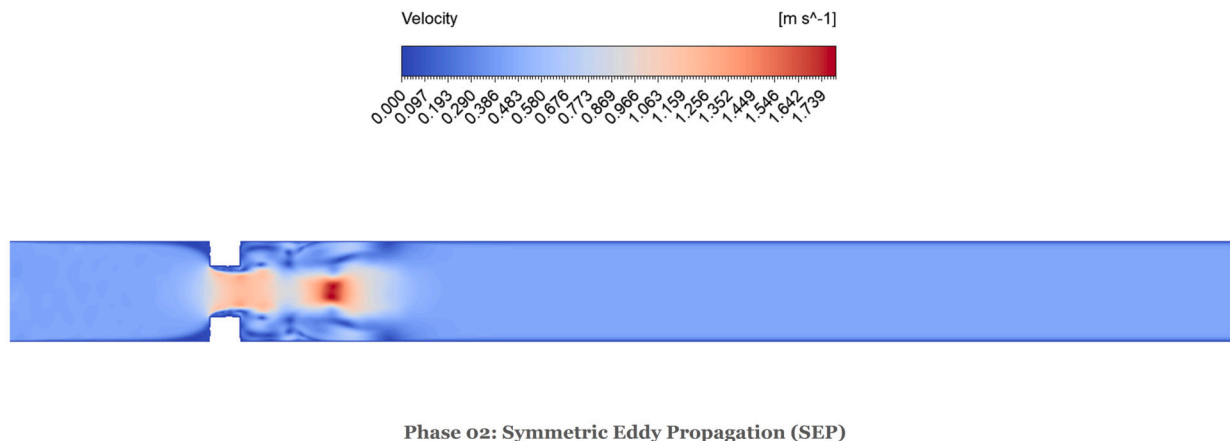


Fig. 7. Symmetric Eddy Propagation phase. It starts at 0.06 sec and ends at 0.1 sec, in general.

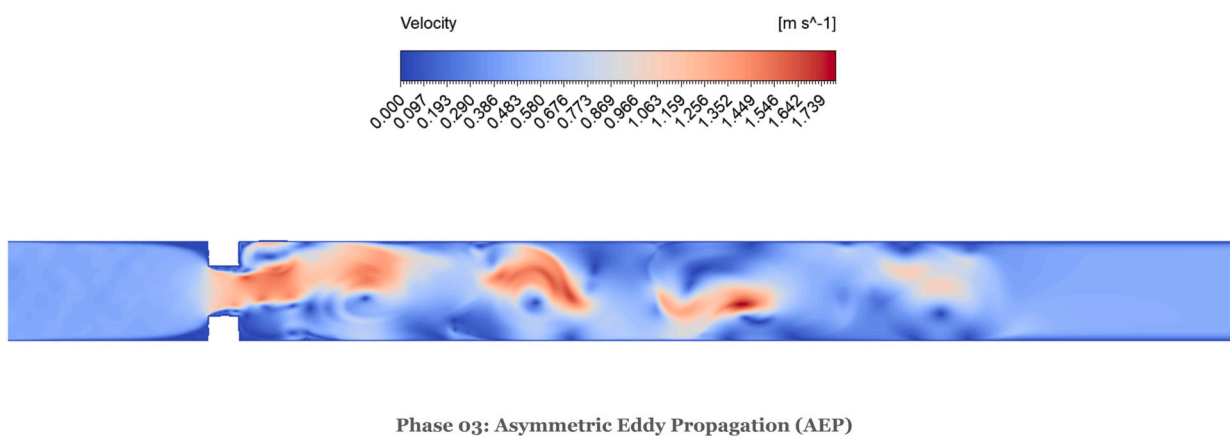


Fig. 8. Asymmetric Eddy Propagation phase. It starts at 0.1 sec and ends at 0.2 sec, in general.

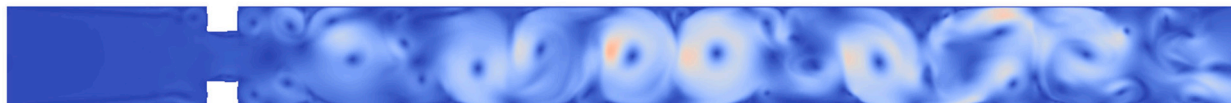
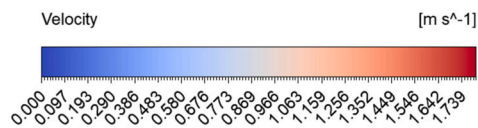
rate in the post-stenotic region. We find that this period coincides perfectly with the KVS for all stenosis cases. While the Q-criterion has been previously linked to vortex structures, cf. [71], its usage (considering the slope of its post-stenotic area-weighted average) to time the onset and duration of the KVS phase is a new result of this study. This is our recommended procedure to accurately identify the corresponding window within the cardiac cycle to probe the acoustic signature of interest to bruits and find a suitable replacement for the break frequency.

Fading Vortex Street (FVS). This phase designates a pattern where the region nearest the stenosis witnesses a fading vortex street while the remainder of the train remains well-formed; see Fig. 11. This phase is induced by the notable decrease in the inlet velocity during this cardiac cycle phase. It last between 0.4 and 0.65 seconds of the 1-second cardiac cycle. Its occurrence is undocumented in the literature on stenotic flow and is a new detail on stenotic flow phases revealed by this LES analysis.

Exiting Vortex Street (EVS). This phase designates the outflow of the shortened (partly faded) vortex street. In this phase, the street's vortex centers also approach the domain's axial line; see Fig. 12. It last between 0.65 and 1 second. Its occurrence is also undocumented in the literature on stenotic flow and is a new detail on stenotic flow phases revealed by this LES analysis.

3.2. Analysis of acoustic signals emitted

As indicated in Fig. 3, using the FW-H method, the associated acoustic signal for stenotic flow can be obtained at a pre-defined receiver located within the acoustic domain externally to the stenosed blood vessel. Noting that heart rate varies with human activity, we recommend subtracting the acoustic signals generated for all stenotic cases first from the acoustic signal for a clean case (non-stenotic) at the same heart rate. The differencing serves to alleviate acoustic signal dependency on heart rate. Moreover, the resulting time-differenced (differential) acoustic signal features the stenosis-induced bruits and their dependence on degree of stenosis more visibly, as can be noted by comparing Figs. 13a–13c. We remark that using differential signals is a new methodical contribution of this study. These differential signals are then input into our spectral analysis.



Phase 04: Karmen Vortex Street (KVS)

Fig. 9. Karman Vortex Street phase. It starts at 0.2 sec and ends at 0.4 sec, in general.

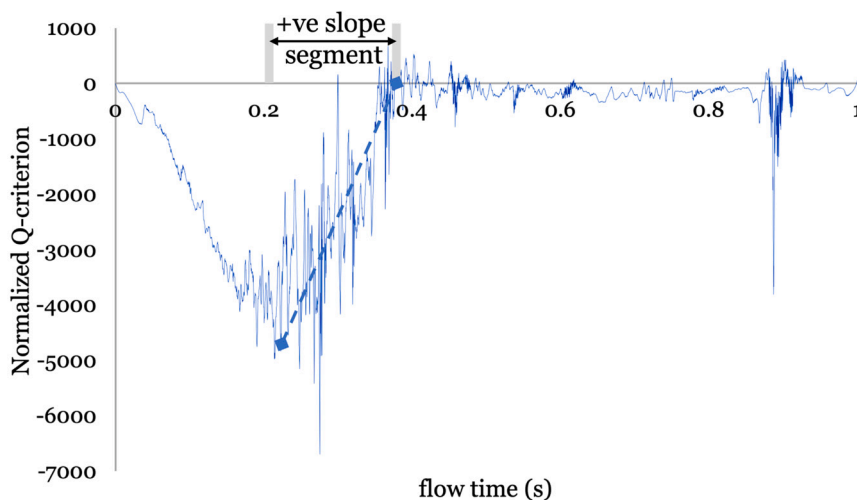
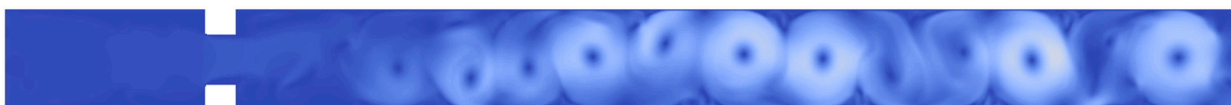
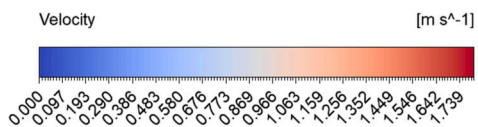
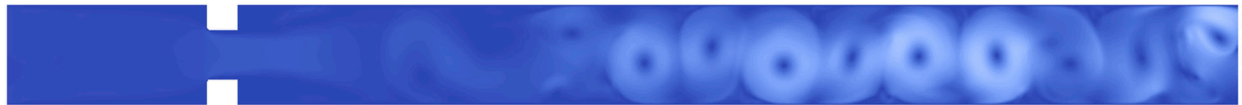
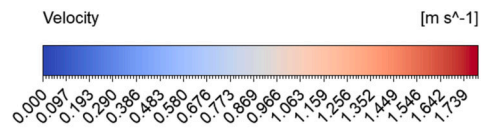


Fig. 10. Karman Vortex Street (phase 4) coincides with the segment of positive slope for the area-weighted average Q-criterion in the post-stenotic region, where rotational flow progressively grows relative to the strain rate.



Phase 05: Fading Vortex Street (FVS)

Fig. 11. Fading Vortex Street phase. It starts at 0.4 sec and ends at 0.65 sec, in general.



Phase 06: Exiting Vortex Street (EVS)

Fig. 12. Exiting Vortex Street phase. It starts at 0.65 sec and ends at 1 sec, in general.

We analyzed the frequency spectrum of the differential acoustic signals for all stenotic simulations; see Figs. 14a–14c for an illustration of such an analysis at 50% stenosis. Generally speaking, the heart rate of 1 Hz will not cancel out from the FFT spectrum since it associates with different pressures in the stenotic and non-stenotic cases. The 1 Hz peak will thus remain irrespective of the degree of stenosis, though its height will increase with an increasing degree of stenosis. This is consistent with the literature, which often cites it as a dominant frequency of vortex shedding for stenosis, cf. [72,73]. We, therefore, seek to identify another characteristic acoustic frequency whose presence arises from any of the six flow phases we identified in the previous section, and which correlates strongly with the degree of stenosis. It should not depend on heart rate, and should enable clinicians to easily quantify the degree of stenosis using stethoscopes. Hence we seek the correlation with any identifiable frequency below the 120 Hz range that distinguishes mild to severe cases.

Specifically, as shown in Fig. 15 for a 50% stenotic case, we segment the differential acoustic signal of the entire cycle (Fig. 15a) per each of the six phases we identified (Figs. 15b–15g). For each segment, FFT is applied, and its dominant frequency is recorded. We recognize that such a simple signal segmentation process introduces artificial time boundary effects that could pollute the corresponding segments of the FFT spectrum. However, these artifacts will not alter a segment's dominant frequencies. We thus ignore this issue in this manuscript.

Based on our analysis of the dominant frequencies for each phase of flow, we have selected the acoustic frequency of vortex shedding (KVS phase) for further analysis. The earliest start time for the KVS phase is 0.2 s (Case 30%), and the latest end time is 0.4 s (Case 80%). The differential acoustic signal for all stenotic cases was thus clipped between these time frames for spectral analysis by FFT. We note that the KVS phase is physiologically associated with the peak systole of a cardiac cycle, which renders the associated CFD flow field especially reliable (least chaotic stage of flow).

Following our CFD-FFT approach, the dominant frequency of vortex shedding within the KVS phase is thus obtained for each stenotic case, as listed in Table 3. As can be seen the dominant frequency is well within the 120 Hz threshold of stethoscopes. As the frequency does not exceed 55 Hz in this study, we recommend selecting an amplified stethoscope [32]. Based on this data, a continuous correlation between the degree of stenosis and the dominant auscultated frequency of vortex shedding (Strouhal number) is constructed; see Fig. 16. We here remark that we could not find similar linear scaling laws in the literature. Instead, scaling laws that are based on the break frequency typically exhibit only little sensitivity to turbulent flow structures [74], with exponents nearing 0.1 (instead of 1) in 2D flows, e.g., [31]. Such laws can only help distinguish mild, moderate, and severe cases since their sensitivity to variations in stenosis percentage is limited by this low exponent. Our proposed definition of the dominant frequency based on von Karman Vortex Street's acoustic signature does away with the break frequency entirely. It accordingly yields a strong linear correlation that clearly distinguishes the continuous degrees of stenosis within an audible range suited for stethoscopes and which is clinically consistent (as shown in our discussion section). In the appendix, all degrees of stenosis we modeled are summarized for completeness.

4. Result discussion and clinical data comparison

Our newly identified KVS-restricted dominant acoustic frequency of vortex shedding thus differs substantially from published alternatives, e.g., the heart rate (1 Hz), cf. [72,73], the break frequency, cf. [18,31]. This newly proposed frequency yields a linear correlation for all stenosis degrees, rendering it considerably more sensitive to clinical variations than the scaling laws based on the break frequency. It thus permits accurate quantification of stenosis beyond the mild, moderate, and severe classifications. More importantly, the frequency identified in this study lies well below the 120 Hz threshold for all stenosis cases (unlike the break frequency), which makes identifying the degree of stenosis easy for clinicians using an electronic stethoscope (instead of resorting to advanced phonoangiography devices).

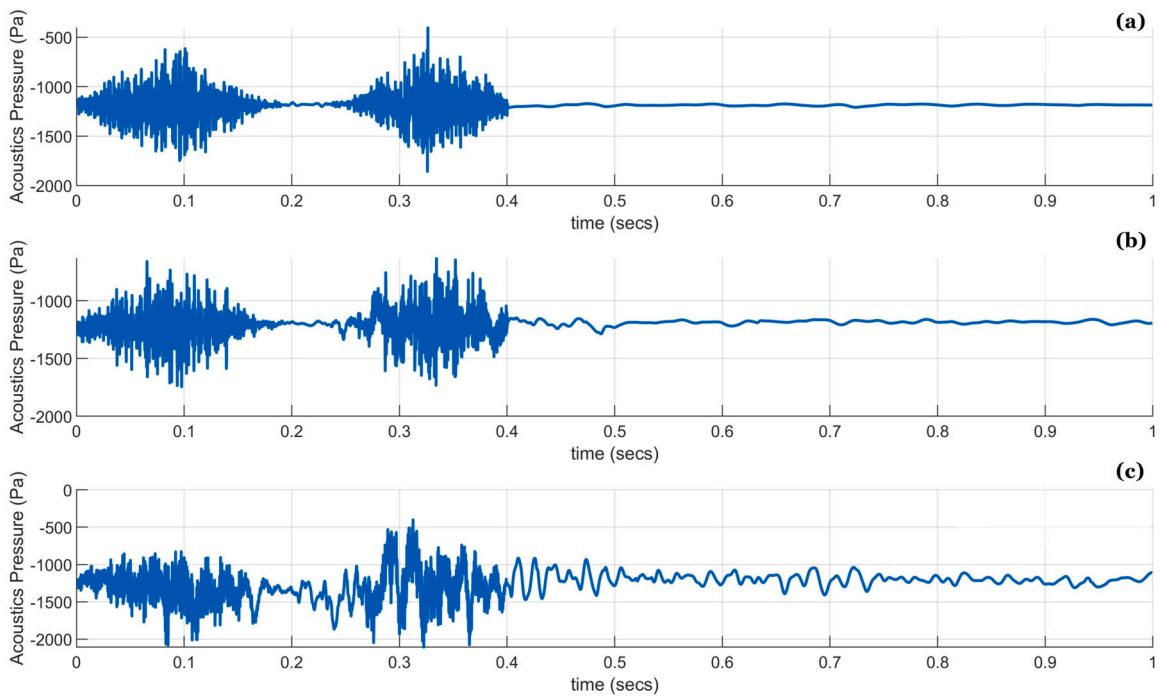


Fig. 13. Differential acoustic pressure signal (Pa) against time (Sec.). Comparison between (a) 30% , (b) 50% , and (c) 80% stenosis cases, subtracted from a non-stenotic signal at the same heart rate (1 Hz).

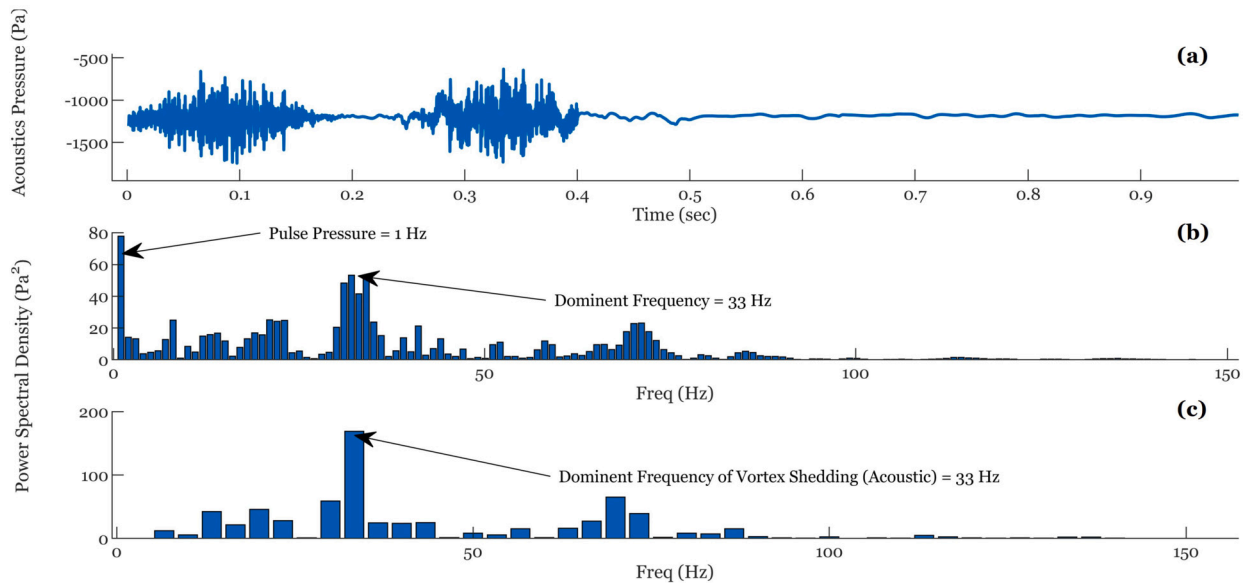


Fig. 14. (a) The differential acoustic pressure signal for 50% stenosis, (b) its transformation to the frequency domain using FFT, and (c) restricting the FFT transformation to the acoustic signature of the KVS phase ($t=0.2$ to $t=0.4$ sec).

Lastly, we benchmark our new correlation against a clinical signal that characterizes a typical stenosis case. The clinical signal is available in audio format at [75]. The case corresponds to a severe case of stenosis (unknown percentage). We thus subtracted this acoustic signal from that of a stenosis-free clinical signal that was also available at [75] for a comparable heart rate. We segmented the differential acoustic signal and picked the KVS times using the Q-criterion. We found the acoustic frequency of vortex shedding to be 55 Hz. Compared with Fig. 16, this corresponds to an approximately 80% degree of stenosis, confirming the clinical assessment of the acoustic signal as severe (i.e., more than 70%). The steps that we followed are summarized in Figs. 17a–17d. We reckon, therefore, that our linear correlation is reasonable and of potential clinical applicability. We include this [link](#), which contains the

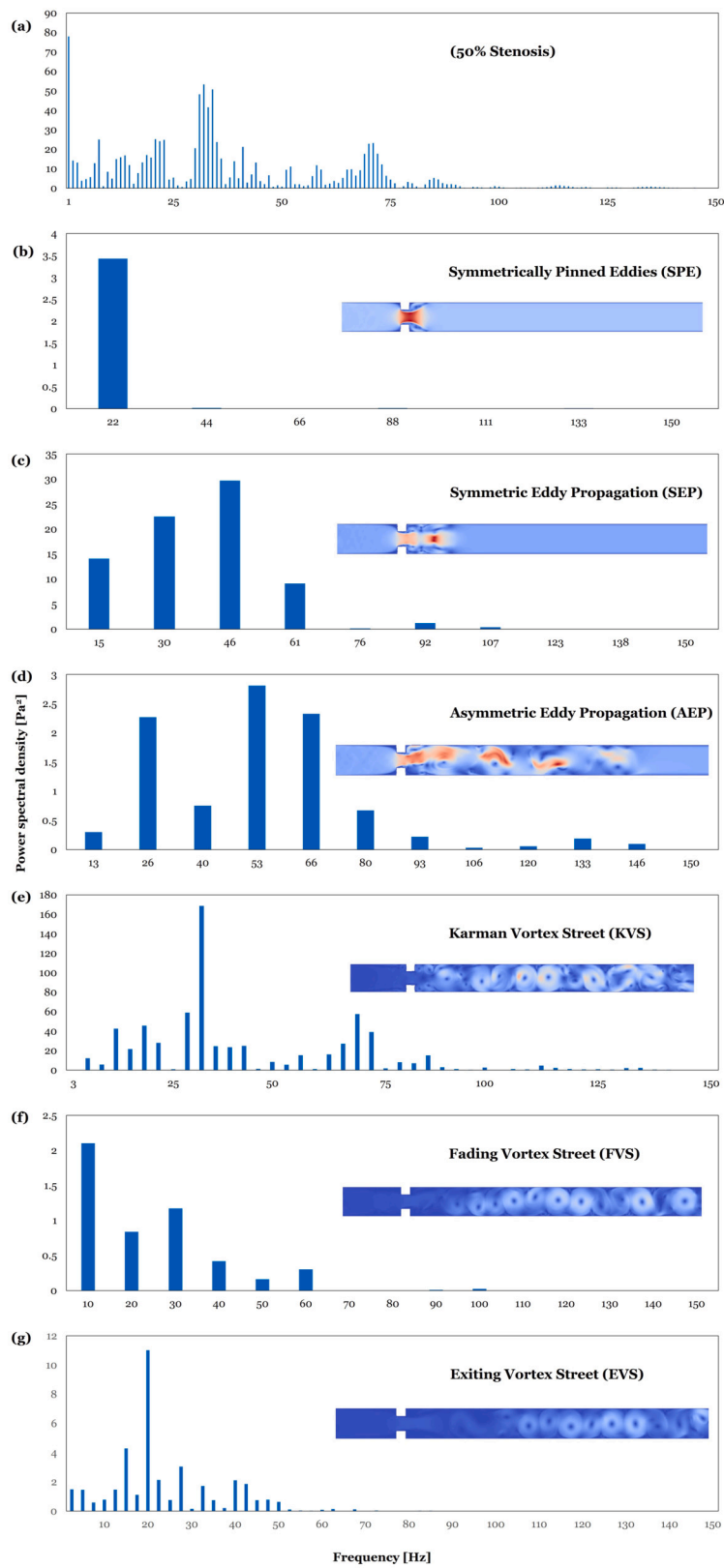


Fig. 15. For the Case of 50% Stenosis, first FFT of the entire acoustic signal is introduced (a), then from (b) to (g), the FFT of each phase is shown. Note that the dominant frequency for each phase is the one with the highest amplitude.

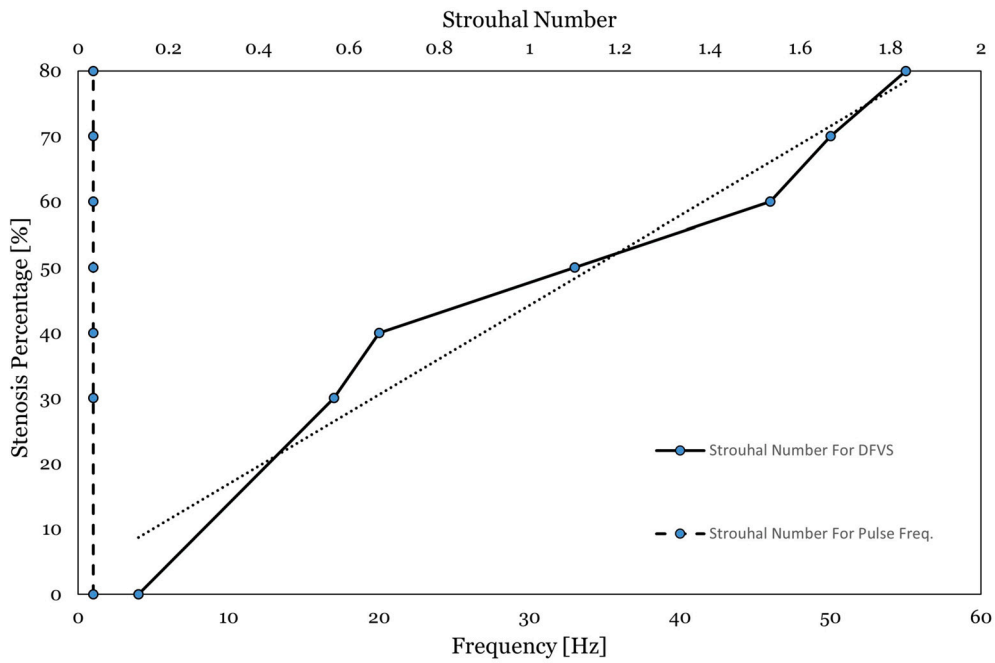


Fig. 16. Dominant frequency of vortex shedding (acoustic) vs. stenosis percentage.

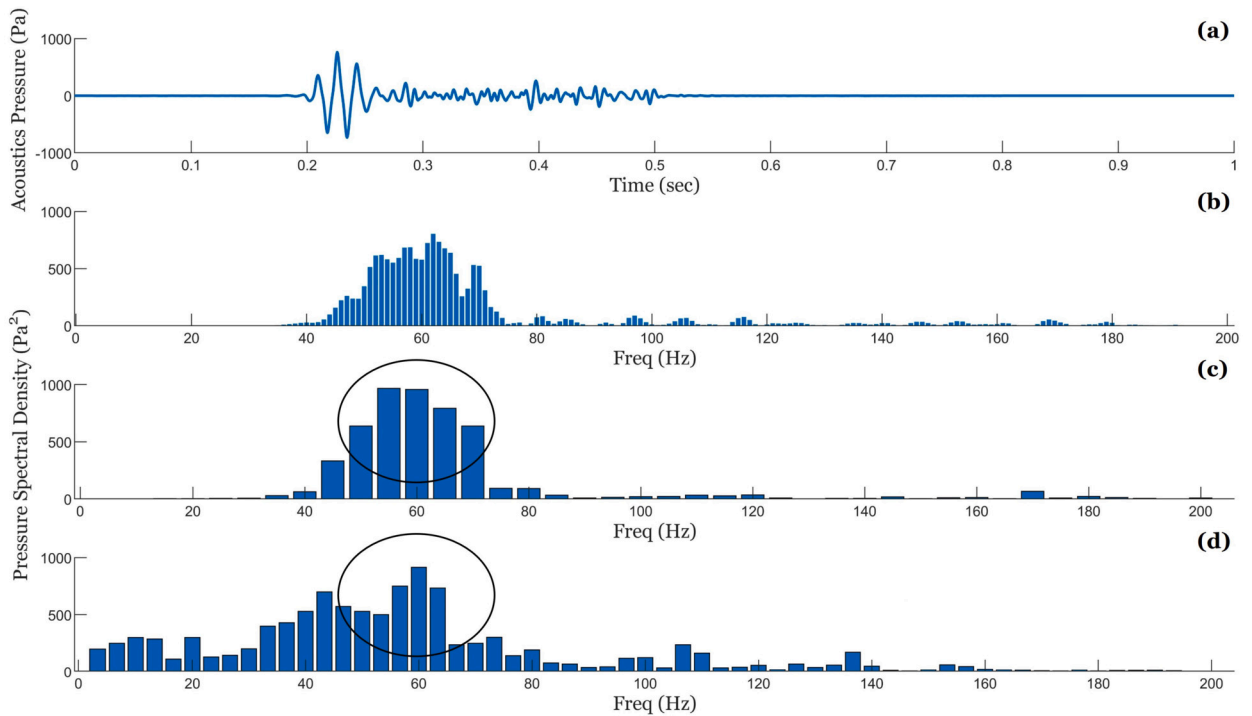


Fig. 17. Clinical differential signal for method validation. (a) shows the differential acoustic signal in the time domain, (b) its FFT, (c) the FFT of the clinical signal restricted to the time-frame of 0.2 s to 0.4 s, and (d) the corresponding FFT of the KVS phase we simulated at 80% stenosis for comparison to the clinical FFT in the same timeframe.

Table 3
Dominant frequency of vortex shedding for each stenosis case.

Stenosis %	DFVS (Acoustic) Hz
0%	4
30%	17
40%	20
50%	33
60%	46
70%	50
80%	55

DFVS: Dominant Frequency of Vortex Shedding

clinical and simulated differential acoustic signals for one cardiac cycle (to be played on auto-repeat), for the readers who wish to compare the similarity of their sounds. As will be apparent to the listener, simple reliance on our auditory sense will not suffice to distinguish the degree of stenosis accurately. This further justifies the need for the CFD-FFT approach we developed herein. Indeed, this approach can be readily extended to analyzing various hemodynamic conditions reported on the PASCAL and PhysioNet 2016 databases to discover other new hemoacoustic correlations.

5. Conclusion

We proposed a new vortex shedding frequency that exhibits a strong linear correlation with the degree of stenosis, aiming to extend the potential of phonoangiography to stethoscope-based diagnostics. Our computational approach is based on CFD-FFT simulation, and a restriction of the acoustic analysis to the von Karman Vortex Street, whose duration we show can be identified in terms of the area-weighted average of the Q-criterion. Per this new analysis, the dominant frequency of vortex shedding was identified to evolve considerably differently from the heart rate or the break frequency and to correlate linearly with the degree of stenosis instead of being raised to the power of 0.1, rendering it quite sensitive to clinical variations in the degree of stenosis (instead of merely classifying stenosis as mild, moderate or severe). We compared our predicted stenosis-frequency correlation to available clinical phonocardiographs and found good agreement with the reported clinical severity assessment. We deem that generalizing our approach to more complex stenotic morphologies, e.g., patient-specific CFD analyses [76–78], and accounting for the influence of surrounding tissue, e.g., [79,80], on the emitted acoustic signal would be of relevance to future research and broader clinical applicability.

CRedit authorship contribution statement

Ahmed M. Ali: Performed the experiments; Analyzed and interpreted the data; Wrote the paper.

Ahmed H. Hafez: Performed the experiments; Wrote the paper.

Khalil Elkhodary, Ph.D.: Conceived and designed the experiments; Analyzed and interpreted the data; Contributed reagents, materials, analysis tools or data; Wrote the paper.

Mohamed El-Morsi: Conceived and designed the experiments; Analyzed and interpreted the data.

Declaration of competing interest

The authors declare that they have no known competing financial interests or personal relationships that could have appeared to influence the work reported in this paper.

Data availability

Data will be made available on request.

Acknowledgement

The authors gratefully acknowledge the support of the American University in Cairo, Grant (RSG1-2020)-SSE-MENG-Dr. Mohamed El-Morsi.

Appendix A. Figs. A.1–A.4

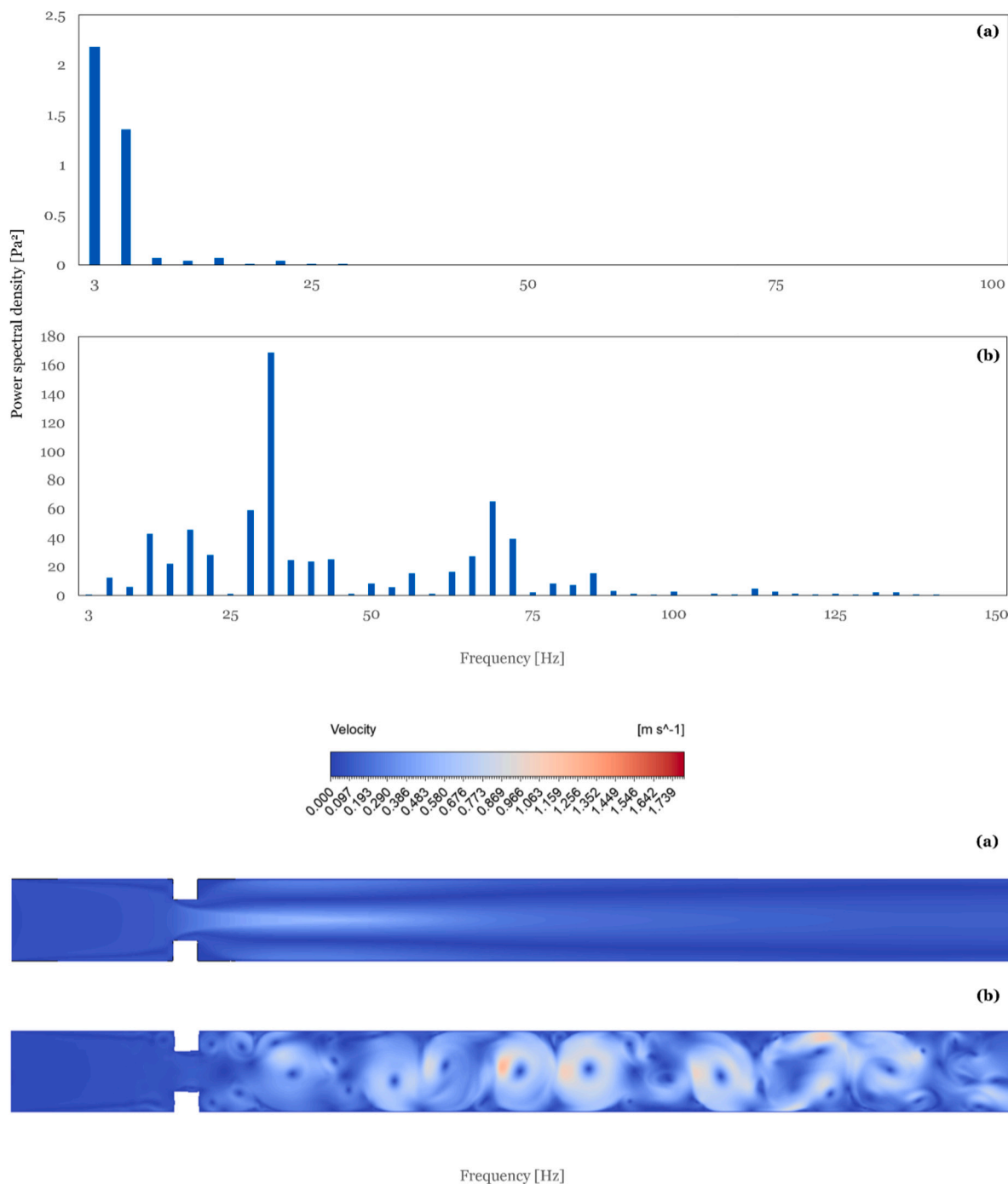


Fig. A.1. FFT and Contour plots of 50% stenosis comparing K-omega (URANS) and LES; (a) represent the results obtained from the k-omega simulation and (b) the results obtained from the LES simulation. URANS yields an incorrect acoustic signature for the KVS phase, being unable to resolve its flow structures.

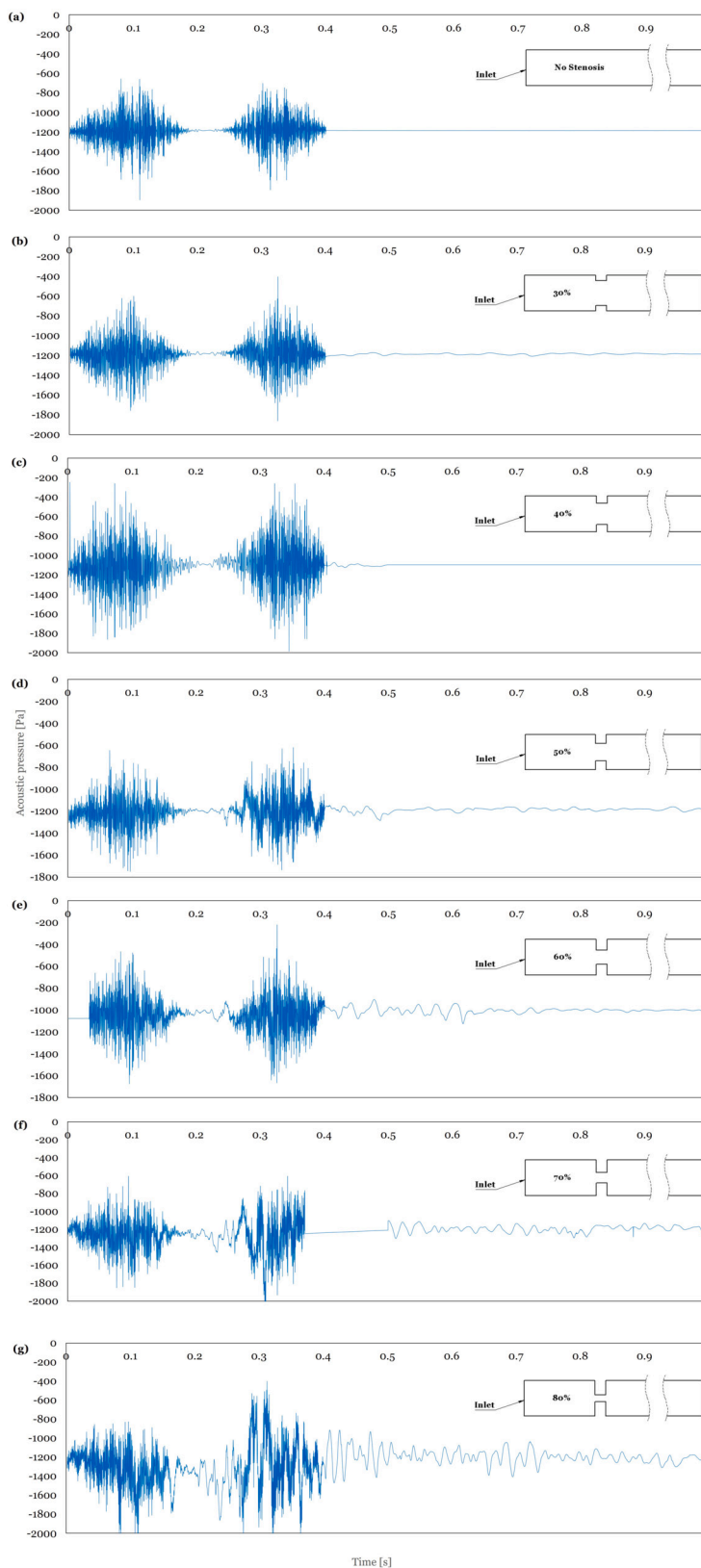


Fig. A.2. Acoustic Pressure Signal vs. Time for stenotic artery, degree of stenosis varies from 30% blockage to 80% blockage.

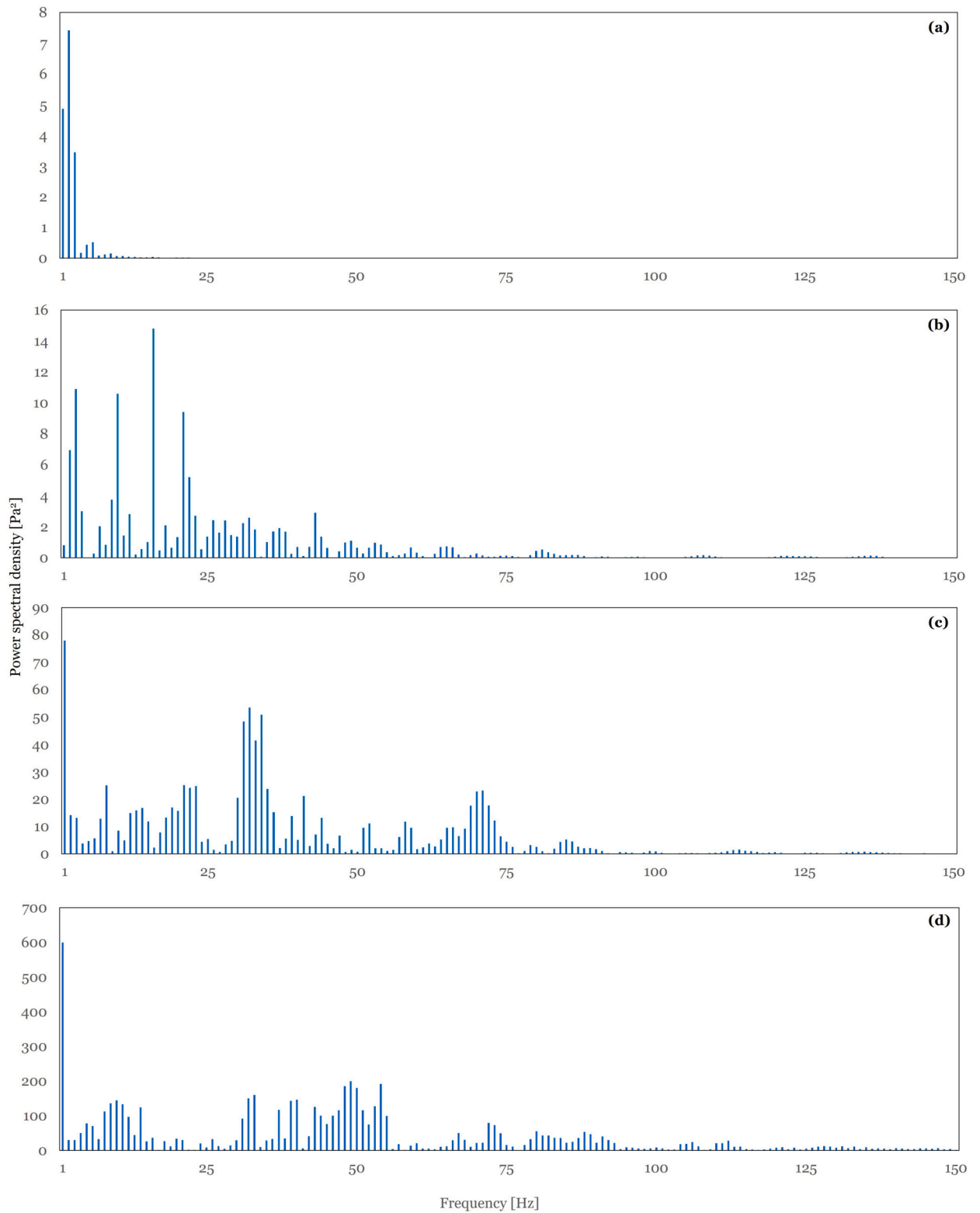


Fig. A.3. FFT of the acoustic pressure signal, (a) No stenosis, (b) 30% Stenosis, (C) 50% Stenosis, (d) 70% Stenosis.

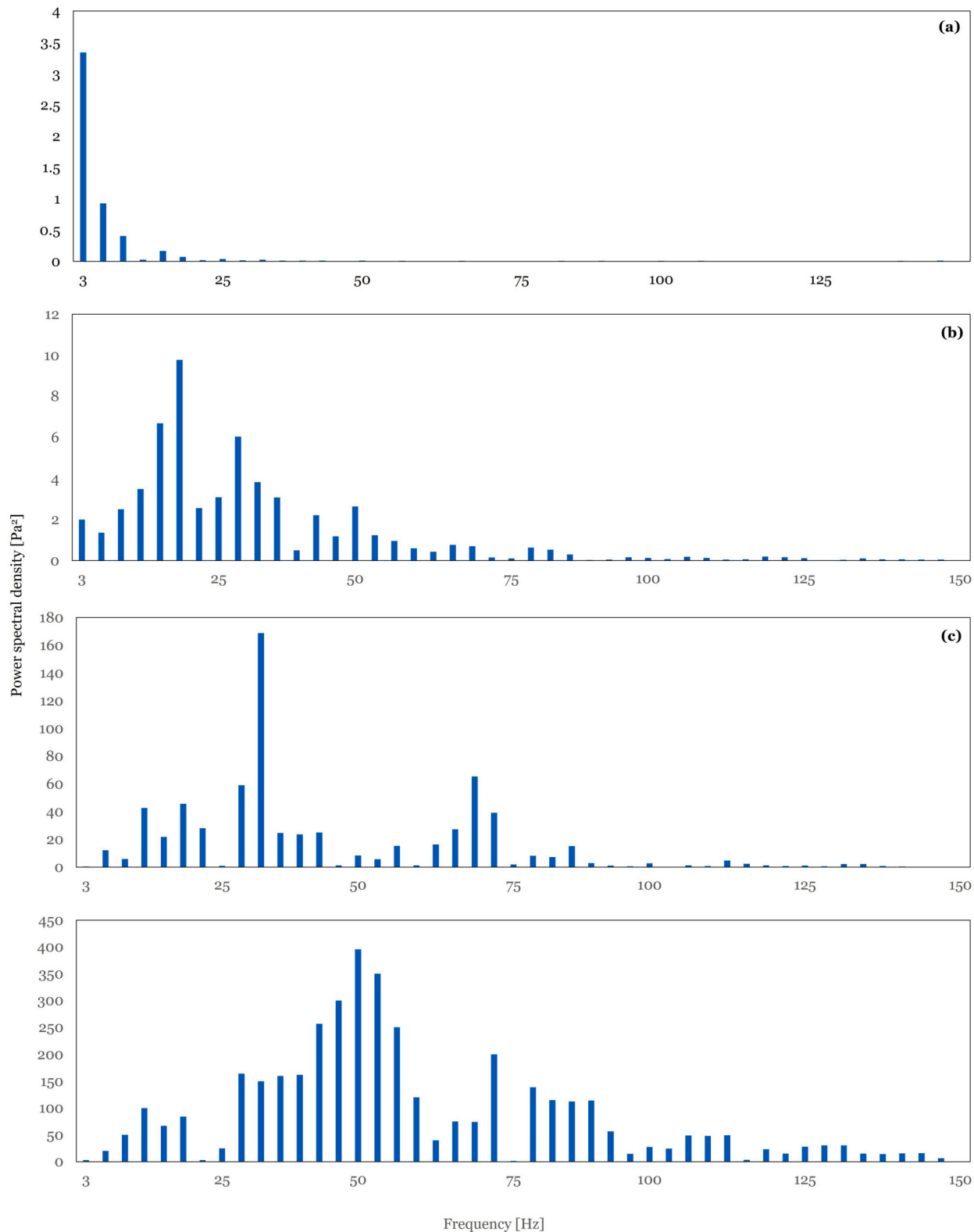


Fig. A.4. FFT of the acoustic pressure signal from time $t=0.2$ s to $t=0.4$ s (vortex start till end), (a) No Stenosis, (b) 30% Stenosis, (C) 50% Stenosis, (d) 70% Stenosis.

References

- [1] K.R. Kanter, B.E. Kogon, P.M. Kirshbom, Supra annular mitral valve replacement in children, *Ann. Thorac. Surg.* 92 (6) (2011) 2221–2229, <https://doi.org/10.1016/j.athoracsur.2011.06.023>, internal-pdf://j.athoracsur.2011.06.023_1.pdf.
- [2] C. Wren, P. Oslizlok, C. Bull, Natural history of supraavalvular aortic stenosis and pulmonary artery stenosis, *J. Am. Coll. Cardiol.* 15 (7) (1990) 1625–1630, [https://doi.org/10.1016/0735-1097\(90\)92837-R](https://doi.org/10.1016/0735-1097(90)92837-R).
- [3] M. Saric, I. Kronzon, Aortic atherosclerosis and embolic events, *Curr. Cardiol. Rep.* 14 (3) (2012) 342–349, <https://doi.org/10.1007/s11886-012-0261-2>, internal-pdf://s11886-012-0261-2_3.pdf.
- [4] I.O. Peshkova, G. Schaefer, E.K. Koltsova, Atherosclerosis and aortic aneurysm - is inflammation a common denominator?, *FEBS J.* 283 (9) (2016) 1636–1652, <https://doi.org/10.1111/febs.13634>, internal-pdf://febs.13634_4.pdf.
- [5] G.-M. von Reutern, M.-W. Goertler, N.M. Bornstein, M.D. Sette, D.H. Evans, M.-W. Goertler, A. Hetzel, M. Kaps, F. Perren, A. Razumovsky, Grading carotid stenosis using ultrasonic methods, *Stroke* 43 (3) (2012) 916–921.
- [6] A. Heidari, K.I. Elkhodary, C. Pop, M. Badran, H. Vali, Y. Abdel-Raouf, S. Torbati, M. Asgharian, R.J. Steele, I. Mahmoudzadeh Kani, et al., Patient-specific finite element analysis of heart failure and the impact of surgical intervention in pulmonary hypertension secondary to mitral valve disease, *Med. Biol. Eng. Comput.* 60 (6) (2022) 1723–1744.
- [7] I. Meissner, B.K. Khandheria, S.G. Sheps, G.L. Schwartz, D.O. Wiebers, J.P. Whisnant, J.L. Covalt, T.M. Petterson, T.J. Christianson, Y. Agmon, Atherosclerosis of the aorta: risk factor, risk marker, or innocent bystander?: A prospective population-based transesophageal echocardiography study, *J. Am. Coll. Cardiol.* 44 (5) (2004) 1018–1024, <https://doi.org/10.1016/j.jacc.2004.05.075>.
- [8] H. Uğuz, A biomedical system based on artificial neural network and principal component analysis for diagnosis of the heart valve diseases, *J. Med. Syst.* 36 (1) (2012) 61–72, <https://doi.org/10.1007/s10916-010-9446-7>.
- [9] R. Rosenhek, U. Klaar, M. Schemper, C. Scholten, M. Heger, H. Gabriel, T. Binder, G. Maurer, H. Baumgartner, Mild and moderate aortic stenosis: natural history and risk stratification by echocardiography, *Eur. Heart J.* 25 (3) (2004) 199–205, <https://doi.org/10.1016/j.ehj.2003.12.002>, internal-pdf://j.ehj.2003.12.002_8.pdf.
- [10] D.G. Blanchard, B.J. Kimura, H.C. Ditttrich, A.N. DeMaria, Transesophageal echocardiography of the aorta, *JAMA* 272 (7) (1994) 546–551.
- [11] M. Cohen-Shelly, Z.L. Attia, P.A. Friedman, S. Ito, B.A. Essayagh, W.-Y. Ko, D.H. Murphree, H.I. Michelena, M. Enriquez-Sarano, R.E. Carter, Electrocardiogram screening for aortic valve stenosis using artificial intelligence, *Eur. Heart J.* 42 (30) (2021) 2885–2896.
- [12] D. Litmanovich, A.A. Bankier, L. Cantin, V. Raptopoulos, P.M. Boiselle, CT and MRI in diseases of the aorta, *Am. J. Roentgenol.* 193 (4) (2009) 928–940.
- [13] L.A. Freeman, P.M. Young, T.A. Foley, E.E. Williamson, C.J. Bruce, K.L. Greason, CT and MRI assessment of the aortic root and ascending aorta, *Am. J. Roentgenol.* 200 (6) (2013) 581–592.
- [14] V. Bapat, M. Thomas, J. Hancock, K. Wilson, First successful trans-catheter aortic valve implantation through ascending aorta using Edwards SAPIEN THV system, *Eur. J. Cardio-Thorac. Surg.* 38 (6) (2010) 811–813.
- [15] T. Sühn, A. Sreenivas, N. Mahmoodian, I. Maldonado, A. Boese, A. Illanes, M. Bloxton, M. Friebe, Design of an auscultation system for phonoangiography and monitoring of carotid artery diseases, in: 2019 41st Annual International Conference of the IEEE Engineering in Medicine and Biology Society (EMBC), IEEE, 2019, pp. 1776–1779.
- [16] F. Azimpour, E. Caldwell, P. Tawfik, S. Duval, R.F. Wilson, Audible coronary artery stenosis, *Am. J. Med.* 129 (5) (2016) 515–521.e3, <https://doi.org/10.1016/j.amjmed.2016.01.015>, <https://www.sciencedirect.com/science/article/pii/S000293431630078X>.
- [17] Z. Sun, K.K. Poh, L.H. Ling, G.S. Hong, C.H. Chew, Acoustic diagnosis of aortic stenosis, *J. Heart Valve Dis.* 14 (2) (2005) 186–194.
- [18] G.W. Duncan, J.O. Gruber, C.F. Dewey, G.S. Myers, R.S. Lees, Evaluation of carotid stenosis by phonoangiography, *N. Engl. J. Med.* 293 (22) (1975) 1124–1128, <https://doi.org/10.1056/NEJM197511272932205>.
- [19] H. Bakhshae, G. Garreau, G. Tognetti, K. Shoele, R. Carrero, T. Kilmar, C. Zhu, W.R. Thompson, J.H. Seo, R. Mittal, A.G. Andreou, Mechanical design, instrumentation and measurements from a hemoacoustic cardiac phantom, in: 2015 49th Annu. Conf. Inf. Sci. Syst., 2015, pp. 1–5.
- [20] R.L. Watrous, W.R. Thompson, S.J. Ackerman, The impact of computer-assisted auscultation on physician referrals of asymptomatic patients with heart murmurs, *Cardiol. Clin.* 31 (2) (2008) 79–83, <https://doi.org/10.1002/clc.20185>.
- [21] J. Semmlow, K. Rahalkar, Acoustic detection of coronary artery disease, <https://doi.org/10.1146/annurev.bioeng.9.060906.151840>, 2007.
- [22] M. Nowak, E. Divo, W.P. Adamczyk, Fluid–structure interaction methods for the progressive anatomical and artificial aortic valve stenosis, *Int. J. Mech. Sci.* 227 (May) (2022) 107410, <https://doi.org/10.1016/j.ijmecsci.2022.107410>.
- [23] N. Shalaby, N. Zenzemi, K. Elkhodary, Simulating the effect of sodium channel blockage on cardiac electromechanics, *proceedings of the institution of mechanical engineers, part H, J. Eng. Med.* 234 (1) (2020) 16–27.
- [24] J.H. Seo, V. Vedula, T. Abraham, R. Mittal, Multiphysics computational models for cardiac flow and virtual cardiography, *Int. J. Numer. Methods Biomed. Eng.* (2013) 850–869, <https://doi.org/10.1002/cnm.2556>.
- [25] S.S. Varghese, S.H. Frankel, P.F. Fischer, Direct numerical simulation of stenotic flows. Part 1. Steady flow, *J. Fluid Mech.* 582 (2007) 253–280, <https://doi.org/10.1017/S0022112007005848>.
- [26] Z. Shen, Z. Yang, Y. Wang, Unsteady correlation between shear layer vorticity and acoustic refraction in low speed open-jet wind tunnel, *Appl. Acoust.* 182 (2021) 108202, <https://doi.org/10.1016/j.apacoust.2021.108202>.
- [27] A. Pathak, P. Samanta, K. Mandana, G. Saha, An improved method to detect coronary artery disease using phonocardiogram signals in noisy environment, *Appl. Acoust.* 164 (2020) 107242, <https://doi.org/10.1016/j.apacoust.2020.107242>.
- [28] Y. Soeta, Y. Bito, Detection of features of prosthetic cardiac valve sound by spectrogram analysis, *Appl. Acoust.* 89 (2015) 28–33, <https://doi.org/10.1016/j.apacoust.2014.09.003>.
- [29] E.R. Mehmet Bilal, Heart sounds classification using convolutional neural network with 1D-local binary pattern and 1D-local ternary pattern features, *Appl. Acoust.* 180 (2021) 108152, <https://doi.org/10.1016/j.apacoust.2021.108152>.
- [30] C. Zhu, J.H. Seo, R. Mittal, Computational modeling and analysis of murmurs generated by modeled aortic stenoses, *J. Biomech. Eng.* 141 (4) (2019), <https://doi.org/10.1115/1.4042765>, internal-pdf://Computational Modeling and Analysis of.pdf.
- [31] J.H. Seo, R. Mittal, A coupled flow-acoustic computational study of bruits from a modeled stenosed artery, *Med. Biol. Eng. Comput.* 50 (2012) 1025–1035.
- [32] A.A. Alanazi, S.R. Atcherson, C.A. Franklin, M.F. Bryan, Frequency responses of conventional and amplified stethoscopes for measuring heart sounds, *Saudi J. Med. Med. Sci.* 8 (2) (2020) 112.
- [33] F. Gao, B. Chen, T. Zhou, H. Luo, Research on the effect of visceral artery aneurysm's cardiac morphological variation on hemodynamic situation based on time-resolved ct-scan and computational fluid dynamics, *Comput. Method Programs Biomed.* (2022) 106928.
- [34] J. Moradicheghamahi, J. Sadeghiseraji, M. Jahangiri, Numerical solution of the Pulsatile, non-Newtonian and turbulent blood flow in a patient specific elastic carotid artery, *Int. J. Mech. Sci.* 150 (October 2017) (2019) 393–403, <https://doi.org/10.1016/j.ijmecsci.2018.10.046>.
- [35] Q. Chi, Y. He, Y. Luan, K. Qin, L. Mu, Numerical analysis of wall shear stress in ascending aorta before tearing in type A aortic dissection, *Comput. Biol. Med.* 89 (2017) 236–247, <https://doi.org/10.1016/j.compbiomed.2017.07.029>.
- [36] P. Sun, S. Bozkurt, E. Sorgun, Computational analyses of aortic blood flow under varying speed CF-LVAD support, *Comput. Biol. Med.* 127 (2020) 104058, <https://doi.org/10.1016/j.compbiomed.2020.104058>.
- [37] R. Savabi, M. Nabaei, S. Farajollahi, N. Fatourae, Fluid structure interaction modeling of aortic arch and carotid bifurcation as the location of baroreceptors, *Int. J. Mech. Sci.* 165 (July 2019) (2020), <https://doi.org/10.1016/j.ijmecsci.2019.105222>.

- [38] T. Lone, A. Alday, R. Zakerzadeh, Numerical analysis of stenoses severity and aortic wall mechanics in patients with supravalvular aortic stenosis, *Comput. Biol. Med.* 135 (June) (2021) 104573, <https://doi.org/10.1016/j.compbimed.2021.104573>.
- [39] P.D. Morris, A. Narracott, H.V. Tengge-Kobliqk, D.A.S. Soto, S. Hsiao, A. Lungu, P. Evans, N.W. Bressloff, P.V. Lawford, D.R. Hose, J.P. Gunn, Computational fluid dynamics modelling in cardiovascular medicine, *Heart* 102 (1) (2016) 18–28, <https://doi.org/10.1136/heartjnl-2015-308044>, internal-pdf://18.full.FD.pdf.
- [40] K.G. Lyras, J. Lee, Comparison of numerical implementations for modelling flow through arterial stenoses, *Int. J. Mech. Sci.* 211 (September) (2021) 106780, <https://doi.org/10.1016/j.ijmesci.2021.106780>.
- [41] S.S. Varghese, S.H. Frankel, Numerical modeling of pulsatile turbulent flow in stenotic vessels, *J. Biomech. Eng.* 125 (4) (2003) 445–460, <https://doi.org/10.1115/1.1589774>, internal-pdf://varghese2003_CFD.pdf.
- [42] A. Scotti, U. Piomelli, Numerical simulation of pulsating turbulent channel flow, *Phys. Fluids* 13 (5) (2001) 1367–1384, <https://doi.org/10.1063/1.1359766>.
- [43] M. Mori, T. Masumoto, K. Ishihara, Study on acoustic, vibration and flow induced noise characteristics of T-shaped pipe with a square cross-section, *Appl. Acoust.* 120 (2017) 137–147, <https://doi.org/10.1016/j.apacoust.2017.01.022>.
- [44] S. Vijaiapurapu, J. Cui, Performance of turbulence models for flows through rough pipes, *Appl. Math. Model.* 34 (6) (2010) 1458–1466, <https://doi.org/10.1016/j.apm.2009.08.029>.
- [45] M.X. Li, J.J. Beech-Brandt, L.R. John, P.R. Hoskins, W.J. Easson, Numerical analysis of pulsatile blood flow and vessel wall mechanics in different degrees of stenoses, *J. Biomech.* 40 (16) (2007) 3715–3724, <https://doi.org/10.1016/j.jbiomech.2007.06.023>, internal-pdf://Numerical analysis of pulsatile blood flow and vessel wall mechanics in different degrees of stenoses.pdf.
- [46] T. Frauenfelder, E. Boutsianis, T. Schertler, L. Husmann, S. Leschka, D. Poulikakos, B. Marincek, H. Alkadhi, In-vivo flow simulation in coronary arteries based on computed tomography datasets: feasibility and initial results, *Eur. Radiol.* 17 (5) (2007) 1291–1300.
- [47] S. Piskin, M. Serdar Celebi, Analysis of the effects of different pulsatile inlet profiles on the hemodynamical properties of blood flow in patient specific carotid artery with stenosis, *Comput. Biol. Med.* 43 (6) (2013) 717–728, <https://doi.org/10.1016/j.compbimed.2013.02.014>.
- [48] D. Xu, S. Warnecke, B. Song, X. Ma, B. Hof, Transition to turbulence in pulsating pipe flow, *J. Fluid Mech.* 831 (2017) 418–432, <https://doi.org/10.1017/jfm.2017.620>, internal-pdf://1709.03738_Re_alpha_values.pdf.
- [49] A.L. Haley, K. Valen-Sendstad, D.A. Steinman, On delayed transition to turbulence in an eccentric stenosis model for clean vs. noisy high-fidelity CFD, *J. Biomech.* 125 (June) (2021) 110588, <https://doi.org/10.1016/j.jbiomech.2021.110588>.
- [50] A.W. Bergersen, M. Mortensen, K. Valen-Sendstad, The FDA nozzle benchmark: “in theory there is no difference between theory and practice, but in practice there is”, *Int. J. Numer. Methods Biomed. Eng.* 35 (1) (2019) 1–10, <https://doi.org/10.1002/cnm.3150>.
- [51] V. Strouhal, Über eine Besondere Art der Tonerregung (on an unusual sort of sound excitation), *Ann. Phys. Chem.* 241 (10) (1878) 216–251, <https://doi.org/10.1002/andp.18782411005>.
- [52] C. Zhu, J.H. Seo, R. Mittal, Computational modeling and analysis of murmurs generated by modeled aortic stenoses, *J. Biomech. Eng.* 141 (4) (2019), <https://doi.org/10.1115/1.4042765>.
- [53] F.M. White, *Fluid Mechanics*, Tata McGraw-Hill Education, 1979.
- [54] A. Redheuil, W.C. Yu, E. Mousseaux, A.A. Harouni, N. Kachenoura, C.O. Wu, D. Bluemke, J.A. Lima, Age-related changes in aortic arch geometry: relationship with proximal aortic function and left ventricular mass and remodeling, *J. Am. Coll. Cardiol.* 58 (12) (2011) 1262–1270, <https://doi.org/10.1016/j.jacc.2011.06.012>, internal-pdf://redheuil2011.pdf.
- [55] S. Poncet, R. Da Soghe, C. Bianchini, S. Viazzo, A. Aubert, Turbulent Couette–Taylor flows with endwall effects: a numerical benchmark, *Int. J. Heat Fluid Flow* 44 (2013) 229–238, <https://doi.org/10.1016/j.ijheatfluidflow.2013.05.018>, <https://www.sciencedirect.com/science/article/pii/S0142727X13001252>.
- [56] B.F. Cadieux, J.A. Domaradzki, T. Sayadi, S. Bose, DNS and LES of separated flows at moderate Reynolds numbers, 2012.
- [57] S. Miyazaki, K. Itatani, T. Furusawa, T. Nishino, M. Sugiyama, Y. Takehara, S. Yasukochi, Validation of numerical simulation methods in aortic arch using 4D flow MRI, *Heart Vessels* 32 (8) (2017) 1032–1044, <https://doi.org/10.1007/s00380-017-0979-2>, internal-pdf://miyazaki2017_CFD.pdf.
- [58] H. Yamamoto, T. Yabuta, Y. Negi, D. Horikawa, K. Kawamura, E. Tamura, K. Tanaka, F. Ishida, Measurement of human blood viscosity using falling needle rheometer and the correlation to the modified Herschel-Bulkley model equation, *Heliyon* 6 (9) (2020) e04792, <https://doi.org/10.1016/j.heliyon.2020.e04792>.
- [59] F. Khalili, P.P. Gamage, H.A. Mansy, Verification of turbulence models for flow in a constricted pipe at low Reynolds number, in: *Proceedings of the Thermal and Fluids Engineering Summer Conference 2018-March, 2018*, pp. 1865–1874, internal-pdf://1803.04313.pdf.
- [60] M. Bathe, R.D. Kamm, A fluid-structure interaction finite element analysis of pulsatile blood flow through a compliant stenotic artery, *J. Biomech. Eng.* 121 (4) (1999) 361–369, <https://doi.org/10.1115/1.2798332>, internal-pdf://MIT-paper.pdf.
- [61] K.B. Chandran, A.P. Yoganathan, S.E. Rittgers, A.P. Yoganathan, S.E. Rittgers, *Biofluid Mechanics the Human Circulation*, Taylor and Francis Group, vol. 43, 2007, internal-pdf://Copy of Biofluid mechanics_the human circulation.pdf.
- [62] S. Qin, B. Wu, J. Liu, W.S. Shiu, Z. Yan, R. Chen, X.C. Cai, Efficient parallel simulation of hemodynamics in patient-specific abdominal aorta with aneurysm, *Comput. Biol. Med.* 136 (July) (2021) 104652, <https://doi.org/10.1016/j.compbimed.2021.104652>.
- [63] J.F. Williams, D.L. Hawkins, Sound generation by turbulence and surfaces in arbitrary motion, *Philos. Trans. R. Soc. Lond. Ser. A, Math. Phys. Sci.* (1969) 321–342.
- [64] M. Souri, A. Mojra, A nexus between active and passive control methods for reduction of aerodynamic noise of circular cylinder, *Int. J. Mech. Sci.* 200 (2021) 106446, <https://doi.org/10.1016/j.ijmesci.2021.106446>.
- [65] A. Kheradvar, G. Pedrizzetti, *Vortex Formation in the Heart*, Springer London, London, 2012, pp. 45–79.
- [66] W.C. Lasher, D.B. Taulbee, On the computation of turbulent backstep flow, *Int. J. Heat Fluid Flow* 13 (1) (1992) 30–40, [https://doi.org/10.1016/0142-727X\(92\)90057-G](https://doi.org/10.1016/0142-727X(92)90057-G).
- [67] H. Jiang, Formation mechanism of a secondary vortex street in a cylinder wake, *J. Fluid Mech.* 915 (2021) A127, <https://doi.org/10.1017/jfm.2021.195>.
- [68] P. Roushan, X.L. Wu, Universal wake structures of Kármán vortex streets in two-dimensional flows, *Phys. Fluids* 17 (7) (2005) 73601, <https://doi.org/10.1063/1.1943469>.
- [69] M.M. Zdravkovich, Smoke observations of the formation of a Kármán vortex street, *J. Fluid Mech.* 37 (3) (1969) 491–496, <https://doi.org/10.1017/S0022112069000681>.
- [70] A.U. Manual, *Ansys, Inc. Modeling, CFX 11*, 2000.
- [71] Y.-n. Zhang, X.-y. Wang, Y.-n. Zhang, C. Liu, Comparisons and analyses of vortex identification between omega method and q criterion, *J. Hydrodyn.* 31 (2019) 224–230.
- [72] C. Lei, L. Cheng, K. Kavanagh, Re-examination of the effect of a plane boundary on force and vortex shedding of a circular cylinder, *J. Wind Eng. Ind. Aerodyn.* 80 (3) (1999) 263–286.
- [73] R. Mittal, H. Dong, M. Bozkurtas, F. Najjar, A. Vargas, A. Von Loebbecke, A versatile sharp interface immersed boundary method for incompressible flows with complex boundaries, *J. Comput. Phys.* 227 (10) (2008) 4825–4852.
- [74] D.L. Bruns, A general theory of the causes of murmurs in the cardiovascular system, *Am. J. Med.* 27 (3) (1959) 360–374.
- [75] University of Washington Department of Medicine, *Advanced Physical Diagnosis. Learning and Teaching at the Bedside (Edition 1), Demonstrations: Heart Sounds and Murmurs*, 2022, <https://depts.washington.edu/physdx/heart/demo.html>.
- [76] S.-y. Pan, M. Ding, J. Huang, Y. Cai, Y.-z. Huang, Airway resistance variation correlates with prognosis of critically ill Covid-19 patients: a computational fluid dynamics study, *Comput. Methods Programs Biomed.* 208 (2021) 106257.
- [77] J. Jiang, C. Li, Y. Hu, C. Li, J. He, X. Leng, J. Xiang, J. Ge, et al., A novel cfd-based computed index of microcirculatory resistance (imr) derived from coronary angiography to assess coronary microcirculation, *Comput. Methods Programs Biomed.* (2022) 106897.

- [78] E.G. Tsega, CFD simulations of respiratory airflow in human upper airways response to walking and running for oral breathing condition, *Heliyon* 8 (8) (2022) e10039, <https://doi.org/10.1016/j.heliyon.2022.e10039>.
- [79] P. Oliazadeh, A. Afsharfard, Analytical study of vibro-acoustic response of a human aorta subjected to an ultrasound wave, *Appl. Acoust.* 175 (2021) 107849, <https://doi.org/10.1016/j.apacoust.2020.107849>.
- [80] F. Khalili, P.P. Gamage, I.A. Meguid, H.A. Mansy, A coupled cfd-fea study of the sound generated in a stenosed artery and transmitted through tissue layers, in: *SoutheastCon 2018*, IEEE, 2018, pp. 1–6.